Doctoral theses at NTNU, 2022:371

Harish Subramanian Gopalakrishnan

Dynamics and stability of autoignition fronts in elementary reheat combustor configurations

NTNU
Norwegian University of Science and Technology

Doctoral thesis

Harish Subramanian Gopalakrishnan

NTNU
Norwegian University of Science and Technology
Thesis for the degree of Philosophiae Doctor
Faculty of Engineering
Department of Energy and Process Engineering

Doctoral theses at NTNU, 2022:371

NTNU

ISBN 978-82-326-6736-9 (printed ver.)
ISBN 978-82-326-5766-7 (electronic ver.)
ISSN 1503-8181 (printed ver.)
ISSN 2703-8084 (electronic ver.)

NTNU
Norwegian University of Science and Technology

Harish Subramanian Gopalakrishnan

Dynamics and stability of autoignition fronts in elementary reheat combustor configurations

Thesis for the degree of Philosophiae Doctor

Trondheim, December 2022

Norwegian University of Science and Technology
Faculty of Engineering
Department of Energy and Process Engineering

NTNU
Norwegian University of
Science and Technology

NTNU
Norwegian University of Science and Technology

Thesis for the degree of Philosophiae Doctor

Faculty of Engineering
Department of Energy and Process Engineering

ISBN 978-82-326-6736-9 (printed ver.)
ISBN 978-82-326-5766-7 (electronic ver.)
ISSN 1503-8181 (printed ver.)
ISSN 2703-8084 (electronic ver.)

Doctoral theses at NTNU, 2022:371

PRINTED IN NORWAY
NO - 1598

NORDIC SWAN ECOLABEL
Printed matter
2041 0731

Printed by Skipnes Kommunikasjon AS

Abstract

Stringent regulations on greenhouse gas emissions from gas turbines used for land-based and aircraft applications has resulted in a gradual transition towards carbon-free fuels such as hydrogen. Conventional single-stage combustor architectures, originally designed to operate on natural gas, face challenges in burning hydrogen efficiently. These challenges basically stem from the high reactivity of the hydrogen fuel, resulting in a risk of flame flashback and consequent damage to the engine components. A staged combustion architecture, containing a propagation-stabilized flame in the first stage and an autoignition-stabilized flame in the second reheat stage, allows for efficient power production both with natural gas and fuels with high hydrogen contents by varying the fuel splits between the first and the second stages.

The fascinating phenomena of combustion instability, which results from the unsteady interactions between the flame dynamics and the acoustic field of the combustion chamber, can result in self-sustained flame and flow oscillations. This undesirable phenomenon, also know as thermoacoustic instability, can result in large amplitude oscillations in the flow quantities such as pressure and heat release rate, which can cause structural damage, loss in performance and can significantly impede stable power generation. Getting insight into the phenomenon of combustion instability in reheat combustors with autoignition-stabilized flames is the main objective of this thesis.

Combustion instability in reheat combustors can be established via many different pathways/mechanisms. This work considers one such 'intrinsic' mechanism where acoustic waves generated by heat release rate oscilla-

tions associated with the autoignition front travel upstream and introduce temperature, pressure and velocity perturbations in the incoming reactant mixture. These flow perturbations modulate the autoignition chemistry and the front kinematics, thereby creating ignition front position and heat release rate oscillations, which, in turn, generate upstream-traveling acoustic disturbances, closing the feedback loop.

In this work, intrinsic thermoacoustic (ITA) oscillations in reheat combustion systems are first investigated by solving the compressible reactive Navier–Stokes and Euler equations in a simple one-dimensional combustor geometry. These computations are used to demonstrate the occurrence of intrinsic thermoacoustic oscillations and characterize the linear stability of the ITA mode. In the second part of this work, modeling tools to enable efficient prediction of the intrinsic thermoacoustic oscillations associated with autoignition fronts in the linear regime are proposed. A simplified flame response framework, based on a Lagrangian treatment of the autoignition process, in combination with a linearized Euler equation (LEE) framework are used to predict the linear stability of the ITA subsystem of the reheat combustor. Both these frameworks are compared to more detailed high-resolution numerical flow computations yielding good comparisons both in the context of flame dynamics and acoustic field prediction. Furthermore, the predictions of the thermoacoustic eigenvalue, which characterize the frequency and growth rates of the thermoacoustic oscillations, from the simplified frameworks show good agreements with the detailed flow computations suggesting that the modeling tools proposed in this work can be used to predict thermoacoustic oscillations in more complex laboratory and industrial scale reheat combustor geometries.

Preface

This thesis is submitted to the Norwegian University of Science and Technology (NTNU) for partial fulfilment of the requirements for the degree of philosophiae doctor. The doctoral work has been carried out in the Thermo Fluids Group at the Department of Energy and Process Engineering (EPT), from September 2019 until October 2022. This work was conducted under the framework of the Reheat2H2 project (project number: 295203), which was supported by the Research Council of Norway (Norges forskningsråd) as part of the NCCS Task 5: Gas turbines.

The research work has been supervised by Associate Professor Jonas P. Moeck and Professor Andrea Gruber. This thesis consists of three chapters and four scientific papers, which are summarized in Chap. 3 and included in full text at the end of the thesis. Of the four papers, three have been published in or presented at scientific journals/international conferences, while one is under consideration for publication in a journal. Listed in chronological order of publication, the articles are:

Article 1

Response of Auto-Ignition-Stabilized Flames to One-Dimensional Disturbances: Intrinsic Response

Harish S. Gopalakrishnan, Andrea Gruber, and Jonas Moeck

Journal of Engineering for Gas Turbines and Power, Volume 143, Issue 12, 2021

https://doi.org/10.1115/1.4052058

Author contributions: JM conceived the idea of representing the evolution of an autoigniting mixture as a collection of independently evolving fluid elements. HSG implemented this idea computationally. AG performed the DNS computations used to validate the Lagrangian framework. HSG wrote the manuscript which was edited and improved by JM and AG. JM and AG supervised the work.

Article 2

Prediction of autoignition-stabilized flame dynamics in a backward-facing step reheat combustor

Harish S. Gopalakrishnan, Tarjei Heggset, Andrea Gruber, and Jonas Moeck

Presented at the Combustion Institute - Canadian Section, Spring Technical Meeting, 2022, Ottawa, Canada.

Author contributions: JM conceived the idea of representing the evolution of an autoigniting mixture as a collection of independently evolving fluid elements. HSG implemented this idea computationally. TH and AG performed the LES computations used to validate the Lagrangian framework. HSG wrote the manuscript which was edited and improved by JM and AG. JM and AG supervised the work.

Article 3

Computation of Intrinsic Instability and Sound Generation from Autoignition Fronts

Harish S. Gopalakrishnan, Andrea Gruber, and Jonas Moeck

Journal of Engineering for Gas Turbines and Power, 2022

https://doi.org/10.1115/1.4055421

Author contributions: HSG implemented the linearized Euler equation framework and developed the compressible Euler code. AG performed the DNS computations used to validate the LEE framework. HSG wrote the manuscript which was edited and improved by JM and AG. JM supervised the work.

Article 4

Computation and prediction of intrinsic thermoacoustic oscillations associated with autoignition fronts

Harish S. Gopalakrishnan, Andrea Gruber, and Jonas Moeck

Under consideration for publication in Combustion and Flame

Author contributions: HSG developed the compressible Euler code and the theoretical formulations. AG performed the DNS computations used to validate the forced Euler computations. HSG wrote the manuscript which was edited and improved by JM and AG. JM supervised the work.

Acknowledgements

First and foremost, I would like to thank my advisor Jonas Moeck for giving me this wonderful opportunity. The past three years have been some of the happiest of my life. Each day was filled with new challenges, new learning and insights. The various discussions that I had with Jonas over the course of this work taught me so many new lessons in acoustics, combustion, numerical methods, CFD and linear stability analysis. I would also like to thank him for giving me full freedom in pursuing my many new (sometimes stupid !) ideas, which have made me a more independent researcher. I have learnt so much from you (both technically and otherwise) and have enjoyed working with you, and can only say thank you for this life-changing opportunity. I hope we will continue to work together in the future.

Second, I would like to thank my co-supervisor Andrea Gruber. Much of the foundation and motivation for this work was laid by his excellent DNS computations on autoignition fronts. I have benefited greatly, over the course of many discussions, from his deep knowledge of combustion and CFD. Once again, thank you for this opportunity.

Next, I would like to thank my parents, without whose love and support, I could not even have crossed the halfway mark of this journey. Thank you for instilling in me a fascination for science right from my childhood and for motivating me to take up this journey. Thank you for your valuable advice and encouragement, which was much needed during tough times.

I have been inspired to take up research mainly because of some great teachers that I have been fortunate to study with during the past. In this regard, I would like to thank Vayalakkara Sivadas, Vaitla Laxman and A.R.

Srikrishnan for sparking my interest in fluid mechanics. Next, the stimulating atmosphere at the Indian Institute of Science motivated me to do a PhD. It was also here that I was introduced to thermoacoustics. Therefore, I would like to thank Santosh Hemchandra and Kiran Manoharan for agreeing to work with me during my master thesis. I would also like to thank Santosh for teaching me all about combustion, programming and hydrodynamic stability. Thanks are also due to my other teachers at IISc: Atanu Mohanty, Arnab Samanta, O.N.Ramesh, Ashwini Ratnoo, D.Sivakumar and Kartik Venkatraman.

I have been fortunate to have attended some great courses during my time here at NTNU, which helped me tremendously in my research. In this regard, I would like to thank Bernhard Müller, Ingve Simonsen, Reidar Kristoffersen and Mikael Lindgren for their excellent teaching. Special thanks to Bernhard for helping me with the spatial filtering when I was having sleepless nights unable to understand why my flow computations blowed up. Your excellent lectures in EP8410 changed the way I think about finite difference schemes. In addition, thank you for always taking interest in my work and my career.

I have been lucky to have worked with a bunch of extremely talented and nice colleagues at the Thermofluids group over the past three years. First, I would like to thank Dirren Govender, Philip Buschmann, Ramgopal Sampath and Srikar Yadala for taking interest in my work. Explaining my work to you has been very beneficial, so thank you for your patience and ideas. I am also grateful to my office mates and colleagues: Tarik, Yi Hao, Frida, Loic, Tong Su, Eirik, Bala, Girish, Yannick, Olav, Ariff, Sourav and Fredrick for the nice times at and away from work. Special thanks to Loic for allowing me to run some of my forced computations on your computer.

Finally, thanks to Eugen, Ingrid, Wenche, Trond, Debbie and Marianne for making my day-to-day work easy and pleasant. Also, many thanks to Laurent Gicquel and Kilian Oberleithner for agreeing to examine my thesis.

Lastly, I am grateful to the almighty, without whose divine and infinite grace, none of this would have been possible.

Friday 11th November, 2022

Harish S. Gopalakrishnan

Contents

List of Tables

List of Figures

Nomenclature

The nomenclature in the attached publications at the end of the thesis can differ from the one given here and can include items that are not listed here.

Abbreviations

1D	one-dimensional
NOx	nitrogen oxides
CFD	computational fluid dynamics
DNS	direct numerical simulations
ITA	intrinsic thermo acoustic
LEE	linearized Euler equations
LES	large eddy simulations
LODI	locally one-dimensional inviscid
MET	mixer exit temperature
NSCBC	Navier–Stokes characteristic boundary conditions

Greek symbols

Δh_c	heat of reaction
$\dot{\omega}_i$	production rate of species 'i'

η	relaxation coefficient at exit boundary
ω	angular frequency
ρ	density
σ	relaxation coefficient at inlet boundary
τ	ignition time
ξ	non-dimensional wave number or Fourier variable

Latin symbols

$\mathscr{L}$	wave amplitudes used in the NSCBC formulation
$\mathscr{S}$	Source terms in the characteristic direction
$\mathscr{W}$	characteristic variables used in the NSCBC formulation
c	speed of sound
$D(s)$	dispersion relation governing the linear dynamics of the ITA feedback
f	Riemann invariant associated with a downstream-traveling acoustic wave
F_i	transfer function relating the integrated heat release rate fluctuations to characteristic waves
g	Riemann invariant associated with an upstream-traveling acoustic wave
G_i	transfer function relating the ignition front position fluctuations to characteristic waves
h	Riemann invariant associated with a downstream-traveling entropy wave
h_i	mass-specific enthalpy of species i
k	wave number of acoustic/entropy wave
M	Mach number
MW	molecular weight of the mixture

p	pressure
Q	integrated heat release rate
q	heat release rate
R	characteristic gas constant of the mixture
R_i	transfer functions governing the reflection of incident acoustic and entropy waves
s	Laplace variable = iω
S_i	transfer functions governing the generation of outgoing characteristics by the unsteady ignition front
T	temperature
t	time
T_i	transfer functions governing the transmission of incident acoustic and entropy waves
u	velocity
x	spatial co-ordinate
X_i	mole fraction of species i
X_{ig}	Ignition front position
Y_i	mass fraction of species i

Modifiers

$(\cdot)'$	fluctuating quantity
$(\cdot)_+$	fluctuations induced by the acoustic wave traveling downstream at the right boundary
$(\cdot)_-$	fluctuations induced by the acoustic wave traveling upstream at the left boundary
$(\cdot)_0$	time-averaged quantity
$(\cdot)_t$	target value of the mean quantities and fluctuations to be maintained at the boundary point

∇	gradient
$\nabla\cdot$	divergence
$\widetilde{(\cdot)}$	Fourier transform

Chapter 1

Introduction

The main objective of this thesis is to get insight into the occurrence of thermoacoustic instabilities in reheat combustors with autoignition-stabilized flames. This chapter is intended to give a brief background on combustion instabilities and discuss the current state of the art in thermoacoustic modeling of reheat combustion systems and consequently, present the objectives and goals of this work. This chapter is subdivided into four sections. Section 1.1 points out the importance of a sequential combustion system for power generation with low-carbon fuels. A brief overview of thermoacoustic instabilities is given in Section 1.2. A discussion of intrinsic thermoacoustic feedback and its relevance to a reheat combustion system is given in Section 1.3. Section 1.4 presents the current state of the art with respect to thermoacoustic modeling of reheat combustors, and Section 1.5 lists the objectives of this work.

1.1 Relevance of a sequential combustion system to gas turbines operating on hydrogen

Gas turbines play an important role in enabling consistent power generation along with renewable sources (Conti et al., 2016). While renewable energy sources like solar and wind are being increasingly used around the world, they do not guarantee consistent power production at all seasons/times. Therefore, renewable sources have to be balanced by technologies which can respond flexibly to both varying load demand and fluctuating energy production. Power production with gas turbines using hydrogen as a fuel is one good candidate for this role, which fits perfectly into so-called Power-to-H_2-to-power schemes.

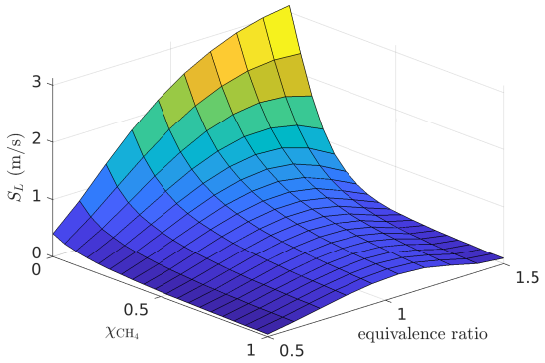

Figure 1.1: Variation of laminar flame speeds of methane–hydrogen–air mixtures with equivalence ratio. The temperature and pressure used for this calculation are 300 K and 1 bar. Adapted from Æsøy (2022).

Hydrogen can be produced using different methods (Dincer and Acar, 2015). First, excess energy from renewables can be used in the electrolysis of water to produce what is termed as *green* hydrogen. Second, steam reforming of methane and the subsequent CO_2 capture and storage produces *blue* hydrogen. The third, and the most commonly used method currently, is the production of hydrogen with steam reforming of methane without carbon capture which is termed as *grey* hydrogen. Therefore, developing technologies which can produce hydrogen with very minimal CO_2 emissions (green or blue hydrogen, for example) combined with methods which efficiently burn hydrogen in gas turbines alongside renewable energy sources can ensure power generation for a sustainable and clean future.

Successful power production using hydrogen in gas turbines necessitates combustor architectures which are capable of burning hydrogen and natural gas interchangeably in a flexible manner. For instance, in the event that the hydrogen/natural gas supply is reduced, we should still be able to burn mixtures containing hydrogen and natural gas in various proportions. Therefore, fuel-flexible combustor technologies are a vital need in the present context.

The main challenge of using hydrogen in a single-stage combustor architecture with propagation-stabilized flames designed to operate on natural gas is the following. Hydrogen, owing to its increased reactivity, i.e., the burning velocity, tends to shift the flame position further upstream in the

combustion chamber (Lieuwen et al., 2008; Bothien et al., 2019c). To get a quantitative idea, Figure 1.1 plots the laminar consumption speed of mixtures of methane and hydrogen at standard conditions. One-dimensional flame speed calculations are performed in Cantera (Goodwin et al., 2022) for the chemical reaction, which, at stoichiometric condition, reads

$$\begin{aligned} x\mathrm{CH_4} + y\mathrm{H_2} + \left(2x + \frac{y}{2}\right)(\mathrm{O_2} + 3.76\mathrm{N_2}) \rightarrow x\mathrm{CO_2} + (2x + y)\,\mathrm{H_2O} \\ + \left(2x + \frac{y}{2}\right)(3.76\mathrm{N_2})\,. \end{aligned} \tag{1.1}$$

A quantity which measures the mole fraction of CH_4 in the fuel stream can be written as

$$\chi_{\mathrm{CH_4}} = \frac{x}{x + y}. \tag{1.2}$$

Figure 1.1 plots the laminar consumption speed of the reactant mixture in Equation (1.1) as a function of hydrogen enrichment and equivalence ratio. It is evident that increasing the hydrogen content increases the flame speed. Therefore, a combustion chamber which was initially designed to operate on natural gas, cannot efficiently operate on hydrogen due to an increased risk of flashback (Yahou et al., 2022). A way to avoid this is to inject less fuel and thereby reduce the flame temperature, moving the flame downstream to its design position. However, this entails a severe reduction in the engine performance. One attractive alternative to overcome this problem is to divide the entire combustion process into two distinct stages using a sequential combustor. An example of such a system presently used is the Ansaldo Energia GT36 constant pressure sequential combustor (Pennell et al., 2017). In a sequential combustor (see Figure 1.2), the first stage flame is stabilized aerodynamically using, for example, vortical structures induced by swirl or bluff-bodies. More fuel is then added to the burnt product mixture exiting the first stage. This vitiated-oxidant mixture, by virtue of its high temperature, spontaneously ignites downstream resulting in the formation of an autoignition front in the second stage. The two contrasting methods of flame-stabilization in the sequential combustor allows for fuel flexibility, minimizing NO_x emissions and maximizing the engine's turndown capability (Ciani et al., 2019; Bothien et al., 2019b,c; Ciani et al., 2020). The next paragraph describes the strategy used in a sequential combustor to reduce pollutant emissions and ensure fuel-flexible operation.

- Reduction of pollutant emissions: At the high operating temperatures experienced during base load, thermal NO_x contributes to the main source of pollutants (Turns et al., 1996). In this scenario, the

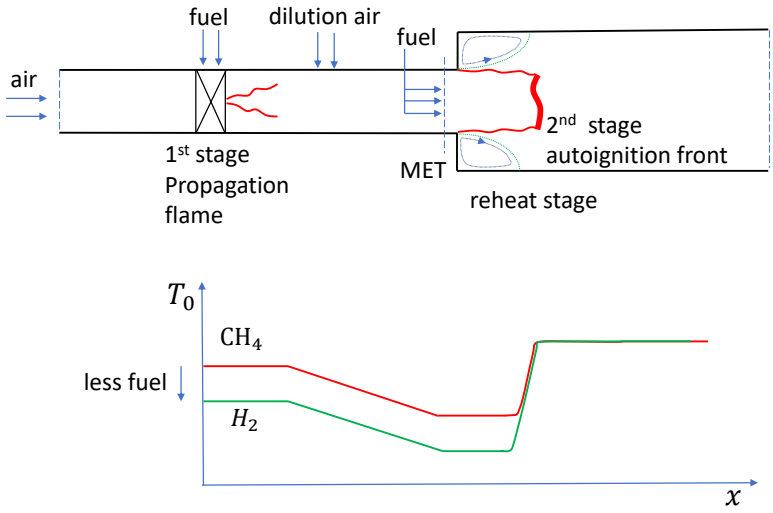

Figure 1.2: Schematic of the two-stage sequential combustion system. The bottom graph shows the strategy used for fuel-flexible operation (adapted from Bothien et al. (2019c)).

mixer exit temperature (MET), which is the inlet temperature at the reheat stage, is reduced causing the autoignition front to be located further downstream resulting in a reduced post-combustion residence time. Conversely, during low part-load operation, the MET is increased resulting in the autoignition front moving substantially upstream, which therefore increases the time required for burnout of carbon monoxide (Bothien et al., 2019c).

- Fuel-flexible operation: To burn a highly reactive fuel such as hydrogen in a sequential burner designed to operate on natural gas, the first stage flame temperature is reduced by injection of less fuel. First of all, this strategy ensures that the propagation-stabilized flame is located at its design position, as the leaner mixture compensates for the increased fuel reactivity (Bothien et al., 2019c). Second, the reduction in the first stage flame temperature also reduces the inlet temperature to the reheat stage (MET), which increases the ignition time associated with the autoigniting mixture. The increased ignition time due to a reduction in the MET compensates for the higher fuel reactivity (see Figure 1.3), maintaining the autoignition-stabilized flame location at its design position (see Figure 1.2).

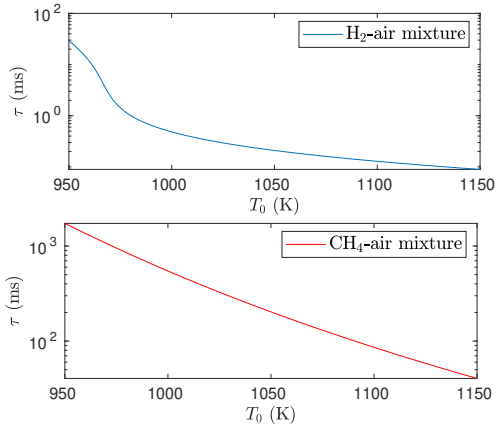

Figure 1.3: Ignition times of vitiated hydrogen–air and methane–air mixtures with temperature. The pressure is 1 bar. The species mass fractions used are taken from Schulz and Noiray (2019) and Aditya et al. (2019). At a given temperature, the ignition time of the hydrogen–air mixture is much smaller than that of the methane–air mixture. Therefore, the MET is reduced for hydrogen–air mixtures to keep the autoignition front position close to the design value.

Combustion instabilities, which manifests due to unsteady interactions involving the flame, the flow dynamics and the acoustic modes of the combustion chamber, are a major problem which affect the stable operation of many combustion systems used for power generation applications. The recent work of Schulz et al. (2019) has demonstrated, using experiments and numerical computations, the occurrence of thermoacoustic combustion instability for a laboratory-scale sequential combustor. Getting insight into combustion dynamics phenomena in sequential combustion systems will be the main focus of this work. The next section gives a brief overview of thermoacoustic instabilities.

1.2 Brief overview of thermoacoustic instabilities

Thermoacoustic oscillations happen due to a feedback loop involving the flow, flame and the acoustic modes of the combustion chamber. In other words, flames respond unsteadily to acoustic waves and unsteady flames generate acoustic waves (Poinsot, 2017). Therefore, a feedback loop involving these two processes can be established resulting in self-sustained flame oscillations, which can cause significant loss in performance and structural damage to engine components (Lieuwen and Yang, 2005).

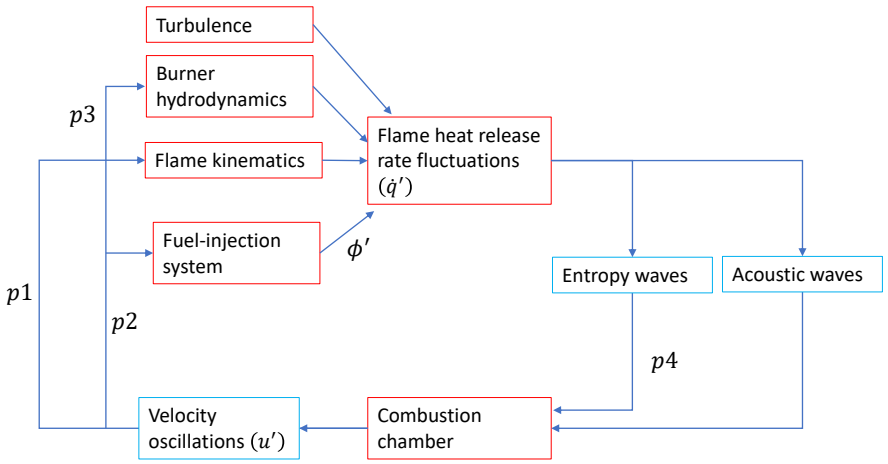

Figure 1.4: Common combustion instability mechanisms in combustors with propagation-stabilized flames. Adapted from Paschereit et al. (2001).

Figure 1.4 summarizes the commonly observed interaction mechanisms resulting in combustion instability in combustors with propagating flames. Propagating flames are usually stabilized at low mean flow Mach numbers. This is because, the kinematic balance between the consumption speed and the local flow velocity dictates the stabilization location of these flames. Flame speeds typically observed for lean mixtures used in low-emission gas turbines are of the order of a few cm/s, resulting in very low values of mean flow Mach numbers. The normalized fluctuations in temperature (T'/T_0) and pressure (p'/p_0) associated with an acoustic wave can be related to the normalized fluctuation in velocity (u'/u_0) as (Dowling, 1995):

$$\begin{aligned} \frac{p'}{p_0} &= \gamma M_0 \frac{u'}{u_0}, \\ \frac{T'}{T_0} &= (\gamma - 1) M_0 \frac{u'}{u_0}, \end{aligned} \tag{1.3}$$

where M_0 is the mean flow Mach number, and γ is the ratio of specific heats. Equation (1.3) suggests that at low Mach numbers characteristic of propagating flames, the magnitudes of the normalized pressure and temperature fluctuations are very small in comparison to the magnitudes of the normalized velocity fluctuations. Therefore, propagating flames are mainly 'velocity-sensitive'. In other words, propagating flames mainly respond to velocity fluctuations upstream of the flame induced by an acoustic wave. In the following, a short summary of the thermoacoustic inter-

action mechanisms of a velocity-sensitive propagation-stabilized flame is given.

- Mechanism $p1$: Heat release rate fluctuations associated with the propagation flame act as a monopole source of sound (Strahle, 1971) generating acoustic disturbances. These acoustic disturbances get reflected from the combustion chamber boundaries and create velocity oscillations locally at the flame. The velocity oscillations created locally at the flame generate flame area oscillations which create heat release rate fluctuations (Schuller et al., 2003) in accordance with the expression

$$\dot{Q}(t) = \int_{\text{flame}} \rho_u S_T^c \Delta h_c dA, \tag{1.4}$$

  which closes the feedback loop. In the above expression, $\dot{Q}$ represents the integrated heat release rate, ρ_u denotes the unburnt gas density, S_T^c is the local consumption speed of the flame, and Δh_c is the unburnt mixture heat of reaction.

- Mechanism p_2: Velocity oscillations induced by the flame-generated acoustic disturbances force the fuel-injection system creating fluctuations in the mixture equivalence ratio (ϕ). For an 'acoustically-stiff' injector, a positive velocity oscillation results in a leaner-mixture and vice-versa. These equivalence ratio fluctuations convect to the flame creating heat release rate oscillations due to a variety of factors as summarized in Shreekrishna et al. (2010). First, ϕ' oscillations create fluctuations in the local flame speed and heat of reaction along the flame surface resulting in heat release rate fluctuations which is a direct effect. Additionally, local flame speed oscillations create flame wrinkles which propagate along the flame creating an indirect non-local influence. The heat release rate oscillations created by these effects, in turn generate acoustic waves which closes the feedback loop.

- Mechanism p_3: Gas turbine combustors typically employ swirl or bluff-bodies to enable flame anchoring (Lefebvre and Ballal, 2010). The mean flow fields associated with these flows are particularly prone to unsteady hydrodynamic phenomenon which can drive flame front oscillations. On the one hand, some of these flows can be convectively unstable. For a convectively unstable flow, disturbances introduced at any point are convected downstream and amplify spatially (Schmid and Henningson, 2001). In such flows, velocity oscillations introduced by the acoustic wave create vortical structures

which convect along the flame creating flame area and heat release rate oscillations which, in turn, generate acoustic waves. Indeed, the work of Oberleithner et al. (2015a) and the work of Hemchandra et al. (2018) has shown that convectively unstable flows which are receptive to acoustic forcing create significant heat release response of the flame. In particular, the frequency at which the flame transfer function peaks coincides with the frequency at which the spatial growth rate of the flow is highest to acoustic velocity perturbations. On the other hand, flows can also be absolutely unstable. In an absolutely unstable flow, disturbances introduced at a point grow both in space and time and eventually, given enough time, contaminate the entire flow. These flows behave as self-excited oscillators with a characteristic frequency. Large regions of absolute instability in a flow can result in global flow oscillations such as the precessing vortex core (Moeck et al., 2012; Oberleithner et al., 2015b). These global flow oscillations can also result in thermoacoustic instability if the frequency associated with them is close to one of the natural acoustic modes of the combustion chamber (Hemchandra et al., 2018). An additional type of hydrodynamic mechanism has been presented in the work of Komarek and Polifke (2010). In their work, the different propagation speeds of axial and azimuthal velocity disturbances associated with a swirl flow in response to an acoustic wave, resulted in fluctuations in swirl number which also creates heat release rate perturbations.

- Mechanism p_4: The unsteady heat release rate oscillations associated with the flame, in addition to generating acoustic disturbances, also generate entropy waves. Entropy waves are temperature inhomogeneities which are convected with the flow. When these entropy waves are accelerated downstream of the combustor by, for example, a nozzle or a turbine blade row, they act as a source of acoustic waves propagating upstream and downstream. This can be deduced by looking at the linearized momentum equation derived for a quasi-1D compressible flow with area change in the famous paper of Marble and Candel (1977) as

$$\left(\frac{\partial}{\partial t}+u_0\frac{\partial}{\partial x}\right)\frac{u'}{u_0}+\frac{c_0^2}{u_0}\frac{\partial}{\partial x}\left(\frac{p'}{\gamma p_0}\right)+\left(2\frac{u'}{u_0}-(\gamma-1)\frac{p'}{\gamma p_0}\right)\frac{du_0}{dx}=\frac{du_0}{dx}\frac{s'}{C_p}, \quad (1.5)$$

which clearly shows that for entropy waves (s') propagating in a nozzle which is characterized by an area change (dA/dx or du_0/dx), a

source term in the RHS of the linearized momentum equation shows up acting as a source of sound. These upstream traveling acoustic waves generated by the accelerating entropy disturbances also perturbs the flame and generates $\dot{Q}'$.

To summarize, self-sustained thermoacoustic oscillations are observed due to two main processes. First, the unsteady flame generating acoustic and entropy disturbances which propagate away from the flame. These flame generated acoustic and entropy disturbances either get reflected from the boundaries or get accelerated through a contraction to produce acoustic disturbances, which in turn force the flame and result in an unsteady flame response. This unsteady response of the flame to an acoustic disturbance can be due to a wide variety of reasons: equivalence ratio fluctuations, swirl number modulation, hydrodynamic flow instabilities, and so on. All these effects can be lumped into a single frequency (ω) dependent function which relates the heat release response of the flame to acoustic forcing. This frequency dependent function, famously called the flame response transfer function (FTF), can be mathematically expressed as

$$\mathscr{F}(\omega) = \frac{\widetilde{\dot{Q}}/\dot{Q}_0}{\widetilde{u}_{\text{ref}}/u_0}, \tag{1.6}$$

which relates the heat release rate perturbations to the velocity perturbations at some reference point. It is vital to realize that the flame transfer function is most meaningful for a linear system since it is amplitude-independent. In other words, the magnitude of the heat release perturbations linearly scale with the magnitude of the velocity perturbations at that frequency. In practice, at large amplitudes of disturbances, a saturation of the flame response amplitude is usually seen (Oberleithner et al., 2015a), at which point an amplitude-dependent describing function is required to describe the flame dynamics (Noiray et al., 2008).

The flame transfer function, for a given combustor and flow configuration, can be determined either using experiments (Æsøy et al., 2020) where acoustic forcing is applied or using high-resolution forced CFD computations in combination with advanced system identification methods (Tay Wo Chong et al., 2010). Once determined, these transfer functions act as the source term to the equations which govern the generation and propagation of acoustic disturbances in a combustor domain (the linearized Euler or Navier–Stokes equations). Under the assumption of an inviscid flow and zero Mach number for the propagation-stabilized flame, these equa-

tions reduce to a single wave equation for pressure, also called as the thermoacoustic Helmholtz equation (Nicoud et al., 2007):

$$\nabla \cdot \left(\frac{1}{\rho_0} \nabla p' \right) - \frac{1}{\gamma p_0} \frac{\partial^2 p'}{\partial t^2} = - \frac{\gamma - 1}{\gamma p_0} \frac{\partial \dot{q}'}{\partial t}. \tag{1.7}$$

The Helmholtz equation, in combination with a flame response model, has shown great success in computing the linear thermoacoustic modes for a wide range of combustor configurations (Silva et al., 2013; Orchini et al., 2020; Buschmann et al., 2020). To determine the thermoacoustic stability eigenvalues, Equation (1.7) is first transformed into the frequency domain by representing the pressure and heat release rate as

$$p'(\mathbf{x}, t) = \widetilde{p}(\mathbf{x}) e^{\mathrm{i}\omega t}. \tag{1.8}$$

When Equation (1.8) is inserted into Equation (1.7), an eigenvalue problem for ω is obtained. The real part of ω gives the frequency of thermoacoustic oscillations, and the imaginary part of ω gives the decay rate of the oscillations.

Another way to qualitatively deduce the occurrence, or otherwise, of thermoacoustic instability in a combustion system is to look at the balance of acoustic energy. An equation for the acoustic energy in zero Mach number flows can be written as (Poinsot and Veynante, 2005)

$$\frac{\partial}{\partial t} \left(\frac{1}{2} \rho_0 \mathbf{u'} \cdot \mathbf{u'} + \frac{1}{2} \frac{p'^2}{\rho_0 c_0^2} \right) + \nabla \cdot (p' \mathbf{u'}) = \frac{\gamma - 1}{\gamma p_0} p' \dot{q}', \tag{1.9}$$

which is applicable at every point in the combustor. A global criterion can be obtained by integrating Equation (1.9) over the entire combustor volume. Applying this integration to Equation (1.9) and using the divergence theorem of Gauss results in

$$\frac{\partial}{\partial t} \int_V \left(\frac{1}{2} \rho_0 \mathbf{u'} \cdot \mathbf{u'} + \frac{1}{2} \frac{p'^2}{\rho_0 c_0^2} \right) dV + \int_A p' \mathbf{u'} \cdot \mathbf{n} \, dA = \int_V \frac{\gamma - 1}{\gamma p_0} p' \dot{q}' dV. \tag{1.10}$$

Equation (1.10) suggests that the time rate of change of acoustic energy in a combustor is due to two reasons. First, due to the flux of the acoustic energy across the boundaries, and second, due to the volumetric production of acoustic energy due to unsteady combustion. Since Equation (1.10) is also time-dependent, it is common to also integrate all terms over one

period of the acoustic oscillation to give a global criterion of thermoacoustic instability for a given combustor. Combustion will be unstable if

$$\frac{\gamma-1}{\gamma p_0}\int_V \frac{1}{\tau}\int_0^\tau p'\dot{q}'\,dt dV > \int_A \frac{1}{\tau}\int_0^\tau p'\mathbf{u}'\cdot\mathbf{n}\,dt dA. \tag{1.11}$$

To summarize, combustion instabilities are a consequence of a coupled feedback loop involving the burner, flame front, combustion chamber and the fuel/air supply. Unsteady heat release rate perturbations associated with the flame generate acoustic waves (Strahle, 1971), which propagate upstream and downstream and get reflected by the chamber boundaries and perturb the flame. If the heat release rate and pressure perturbations constructively interfere such that the driving term is greater than the flux of the acoustic energy at the boundaries [Equation (1.11)], an instability is favoured. In this established framework of understanding, thermoacoustic instability is thought of as the coupling between the flame dynamics and the resonant acoustic modes of the combustion chamber. Therefore, instability cannot be established in a system with fully non-reflecting boundaries.

The pivotal works of Hoeijmakers et al. (2014), Emmert et al. (2015) and Bomberg et al. (2015) showed that thermoacoustic instabilities can be established even in a system with fully non-reflecting boundaries. The fundamental mechanism for these 'flame-intrinsic' thermoacoustic instabilities can be deduced by going back to Figure 1.4. The block 'combustion chamber' represents the reflection of the flame-generated acoustic disturbances which consequently create velocity oscillations locally at the flame and at the fuel-injector or the swirler. However, it is easy to deduce that these velocity oscillations can also be created due to the upstream traveling acoustic disturbances generated by the flame and do not essentially require reflection from the boundaries. Therefore, upstream-traveling acoustic disturbances generated by the flame can perturb the fuel-injection system or perturb the shear layers resulting in equivalence ratio and vorticity fluctuations which convect to the flame and create a flame response, which closes the feedback loop. This intrinsic thermoacoustic (ITA) feedback mechanism will be the primary focus of this work.

1.3 Intrinsic thermoacoustic (ITA) feedback

This section serves to introduce the reader to intrinsic thermoacoustic feedback. The ITA feedback is schematically depicted in Figure 1.5 for a velocity-sensitive propagation-stabilized flame. The ITA feedback occurs as a res-

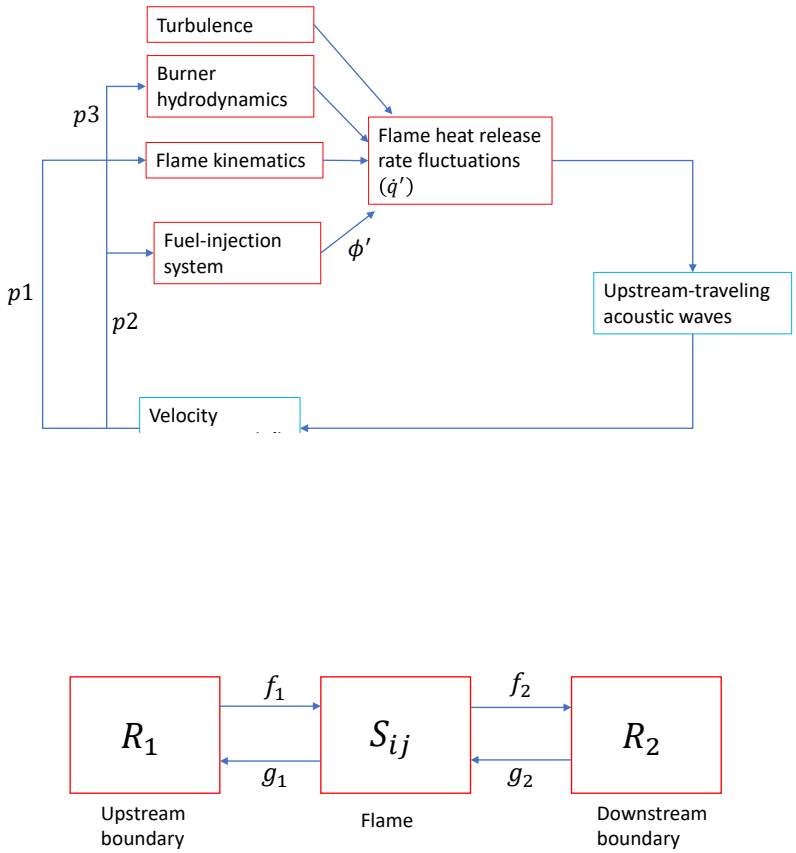

Figure 1.6: Block diagram of a simple thermoacoustic system consisting of a flame and the boundaries. Adapted from Hoeijmakers et al. (2014).

ult of interactions between the upstream-traveling acoustic disturbances generated by the unsteady flame and the flame response, in turn, created by the velocity oscillations induced by these disturbances. The presence of intrinsic thermoacoustic modes are now shown, via a simple analytical framework, for an elementary thermoacoustic system consisting of a flame and the boundaries (see Figure 1.6). Much of the material presented in this section is adapted from Hoeijmakers et al. (2014) and Emmert et al. (2015) with minor deviations with regards to the nomenclature.

The simple thermoacoustic system that we consider is depicted in Figure 1.6. The system is composed of the flame, which is characterized by the scattering matrix. The scattering matrix relates the emanating charac-

teristics to the incident characteristics, and can be written as

$$\begin{bmatrix} f_2 \\ g_1 \end{bmatrix} = \begin{bmatrix} S_{11} & S_{12} \\ S_{21} & S_{22} \end{bmatrix} \begin{bmatrix} f_1 \\ g_2 \end{bmatrix}, \tag{1.12}$$

where $f = \frac{1}{2}(p' + \rho_0 c_0 u')$ denotes the downstream propagating characteristic, and $g = \frac{1}{2}(p' - \rho_0 c_0 u')$ denotes the upstream propagating characteristic. In addition, the upstream and downstream boundaries are characterized by the reflection coefficients which relate the reflected to the incident wave:

$$\begin{aligned} f_1 &= R_1 g_1, \\ g_2 &= R_2 f_2. \end{aligned} \tag{1.13}$$

Equations (1.12) and (1.13) can be combined to form the matrix equation for the complete system as

$$\begin{bmatrix} -1 & R_1 & 0 & 0 \\ 0 & 0 & -R_2 & 1 \\ S_{11} & 0 & -1 & S_{12} \\ S_{21} & -1 & 0 & S_{22} \end{bmatrix} \begin{bmatrix} f_1 \\ g_1 \\ f_2 \\ g_2 \end{bmatrix} = 0. \tag{1.14}$$

For non-trivial solutions, the determinant of the matrix in Equation (1.14) should be zero, which gives the thermoacoustic eigenmodes of the complete system. In the following, however, our main interest is in the intrinsic thermoacoustic sub-system of Figure 1.6, which is only composed of the flame and the associated acoustic waves propagating upstream and downstream. Therefore, our main focus only lies in the scattering matrix [Equation (1.12)] which relates the outgoing characteristics to the incoming characteristics associated with only the burner and flame.

To investigate the occurrence of intrinsic thermoacoustic modes, a one-dimensional flame placed in a combustor with fully non-reflecting boundaries is considered in Figure 1.7. As such, Figure 1.7 represents a generic one-dimensional flow at non-negligible values of Mach numbers where hot spots created at the unsteady flame are convected with the mean flow. In the limit of vanishing Mach number, the flow, at least in the sense of acoustic wave propagation, is treated as frozen and only acoustic waves travel

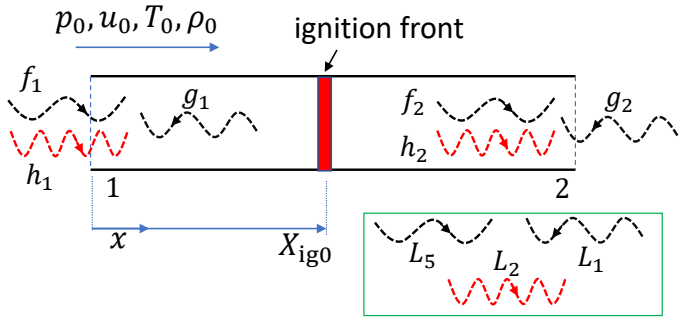

Figure 1.7: Schematic of the one-dimensional combustor used for all computations in the present work. The various waves propagating in the domain are shown. The green box shows the waves nomenclature adopted in the NSCBC formulation. Waves coloured in black are acoustic, while the ones coloured in red are entropic.

upstream and downstream (Bauerheim et al., 2015). At this low Mach number limit, the equations governing the propagation and generation of acoustic waves across the flame are given by (Kopitz and Polifke, 2008):

$$\frac{p_2'}{\rho_{02}c_{02}} = \zeta \frac{p_1'}{\rho_{01}c_{01}}, \qquad u_2' = u_1' + \theta u_{01} \frac{\dot{Q}'}{\dot{Q}_0}, \tag{1.15}$$

where the subscript '1' represents quantities in the unburnt side, and the subscript '2' denotes quantities in the burnt side. The fluctuations are denoted by the primed ()′ symbols and the mean quantities are denoted by the $()_0$ symbols. Additionally, $\zeta = \rho_{01}c_{01}/\rho_{02}c_{02}$ denotes the ratio of specific impedances, and $\theta = T_{02}/T_{01} - 1$ denotes the dimensionless increase in temperature. At low Mach numbers, we can relate θ and ζ as

$$\theta = \zeta^2 - 1. \tag{1.16}$$

Equation (1.15) is a direct consequence of the linearization of the 1D momentum and energy balance Rankine–Hugoniot jump conditions for a stationary heat source at low Mach numbers. The mass balance equation is relevant only for non-negligible Mach numbers as shown in the work of Bauerheim et al. (2015), and is therefore neglected in the present scenario. The pressure and velocity fluctuations in Equation (1.15) are obtained from the acoustic wave ansatz (Dowling, 1995).

In region 1:

$$\begin{aligned} p_1'(x,t) &= \mathrm{e}^{\mathrm{i}\omega t}\left(f_1\mathrm{e}^{-\mathrm{i}\omega x/(c_{01}+u_{01})} + g_1\mathrm{e}^{\mathrm{i}\omega x/(c_{01}-u_{01})}\right), \\ u_1'(x,t) &= \mathrm{e}^{\mathrm{i}\omega t}\left(\frac{f_1}{\rho_{01}c_{01}}\mathrm{e}^{-\mathrm{i}\omega x/(c_{01}+u_{01})} - \frac{g_1}{\rho_{01}c_{01}}\mathrm{e}^{\mathrm{i}\omega x/(c_{01}-u_{01})}\right). \end{aligned} \tag{1.17}$$

In region 2:

$$\begin{aligned} p_2'(x,t) &= \mathrm{e}^{\mathrm{i}\omega t}\left(f_2\mathrm{e}^{-\mathrm{i}\omega (x-l)/(c_{02}+u_{02})} + g_2\mathrm{e}^{\mathrm{i}\omega (x-l)/(c_{02}-u_{02})}\right), \\ u_2'(x,t) &= \mathrm{e}^{\mathrm{i}\omega t}\left(\frac{f_2}{\rho_{02}c_{02}}\mathrm{e}^{-\mathrm{i}\omega (x-l)/(c_{02}+u_{02})} - \frac{g_2}{\rho_{02}c_{02}}\mathrm{e}^{\mathrm{i}\omega (x-l)/(c_{02}-u_{02})}\right), \end{aligned} \tag{1.18}$$

where the characteristic waves f_1 and g_1 are measured at the combustor inlet ($x = 0$), and the characteristic waves f_2 and g_2 are measured at the combustor exit ($x = l$). The final piece of the puzzle is to relate the heat release rate perturbations in Equation (1.15) to the characteristic waves. This is done using Equation (1.6), where the heat release rate perturbations are related to the velocity perturbations just upstream of the flame with a frequency dependent function $\mathscr{F}$. Equations (1.17) and (1.18) evaluated at the mean flame location ($x = X_{\mathrm{ig}0}$) together with Equation (1.6) are substituted into Equation (1.15) to give

$$\begin{aligned} &\begin{bmatrix} \frac{e^{-\mathrm{i}\omega(X_{\mathrm{ig}0}-l)/(c_{02}+u_{02})}}{\rho_{02}c_{02}} & -\zeta\frac{e^{\mathrm{i}\omega X_{\mathrm{ig}0}/(c_{01}-u_{01})}}{\rho_{01}c_{01}} \\ \frac{e^{-\mathrm{i}\omega(X_{\mathrm{ig}0}-l)/(c_{02}+u_{02})}}{\rho_{02}c_{02}} & (1+\theta\mathscr{F})\frac{e^{\mathrm{i}\omega X_{\mathrm{ig}0}/(c_{01}-u_{01})}}{\rho_{01}c_{01}} \end{bmatrix}\begin{bmatrix} f_2 \\ g_1 \end{bmatrix} \\ &= \begin{bmatrix} \zeta\frac{e^{-\mathrm{i}\omega X_{\mathrm{ig}0}/(c_{01}+u_{01})}}{\rho_{01}c_{01}} & -\frac{e^{\mathrm{i}\omega(X_{\mathrm{ig}0}-l)/(c_{02}-u_{02})}}{\rho_{02}c_{02}} \\ (1+\theta\mathscr{F})\frac{e^{-\mathrm{i}\omega X_{\mathrm{ig}0}/(c_{01}+u_{01})}}{\rho_{01}c_{01}} & \frac{e^{\mathrm{i}\omega(X_{\mathrm{ig}0}-l)/(c_{02}-u_{02})}}{\rho_{02}c_{02}} \end{bmatrix}\begin{bmatrix} f_1 \\ g_2 \end{bmatrix}. \end{aligned} \tag{1.19}$$

The scattering matrix associated with the flame can be obtained from equation (1.19) by multiplying both sides by the inverse of the matrix in the LHS. This process reveals that all the elements of the scattering matrix have a common set of poles (s), which are obtained by solving the dispersion relation

$$1 + \zeta + \theta\mathscr{F}(s) = 0, \tag{1.20}$$

where s is the Laplace variable, which can be related to ω as $s = \mathrm{i}\omega$.

The poles of the scattering matrix are very important for the ITA feedback because, from Equation (1.12), at these frequencies an infinitesimal forcing applied onto the system (either by the wave f_1 or g_2, for example) creates significantly large system responses. This means that an internal resonance happens within the system at that frequency. In other words, the applied forcing resonates with the ITA mode leading to large system responses. Indeed, the works of Hoeijmakers et al. (2014) and Bomberg et al. (2015) have shown that the poles of the scattering matrix are the eigenvalues associated with the intrinsic thermoacoustic feedback.

Equation (1.20) can be analytically solved for s by assuming a simple $n - \tau$ model for the flame response given by $\mathcal{F} = ne^{-s\tau}$, which yields the poles

$$s = \frac{1}{\tau} \ln\left(\frac{n\theta}{1+\zeta}\right) + \mathrm{i}\frac{(2k+1)\pi}{\tau}, \tag{1.21}$$

where k is the set of integers $0, 1, 2, \cdots$

Therefore, from Equation (1.21), intrinsic thermoacoustic instability is expected to occur if $\mathrm{Re}(s) > 0$, which gives the limiting condition for the flame response gain as

$$n > \frac{1+\zeta}{\theta}, \tag{1.22}$$

which implies that the ITA mode is unstable if the flame response gain reaches above a certain critical value.

Next, we discuss the importance of intrinsic thermoacoustic feedback for autoignition fronts. Autoignition fronts reside at locations in the combustor where the ignition time of the reactant mixture is equal to the residence time. Unlike the case of a propagating flame where the advection–diffusion–reaction balance governs the flame position to leading order, the balance between the advective and the chemical time scales governs the location of an autoignition front. In Figure 1.7, which depicts an autoignition front stabilized in a one-dimensional combustor, the ignition location (X_{ig0}) is given by the balance

$$\tau_{\mathrm{ig}} = \tau_{\mathrm{res}}, \tag{1.23}$$

where τ_{res} is the residence time, and τ_{ig} is the mixture ignition time. Typical ignition times of vitiated hydrogen–air mixtures at reheat conditions are usually very small, i.e., of the order of a few milliseconds or less. At

these conditions, mean flow velocities of the order of a few hundred m/s are required to maintain the ignition front at desirable locations inside the combustor, which correspond to non-negligible values of Mach numbers (0.25 – 0.3). At such finite values of Mach numbers, the normalized pressure and temperature fluctuations have comparable magnitudes to the normalized velocity oscillations [Equation (1.3)]. The pressure and temperature oscillations induced by the upstream-traveling acoustic waves modulate the chemical kinetic processes associated with spontaneous ignition, which modulates the ignition time of the reactant mixture, and therefore the ignition front position, over one cycle of acoustic forcing. The fluctuations in the ignition front position create significant oscillations in the global and local heat release rate (Gant et al., 2020b; Gopalakrishnan et al., 2021), which in turn induces upstream-traveling acoustic disturbances (Chen et al., 2016), thereby closing the feedback loop.

Figure 1.8(a) plots the variation of the ignition time (τ) of a reactant mixture with temperature (T). A constant-pressure reactor calculation in Cantera (Goodwin et al., 2022) with static variations in temperature is used to generate Figure 1.8(a). As expected, an increase in temperature accelerates the ignition chemistry and results in a decrease in ignition time. A parameter (ψ) can now be defined to quantify the sensitivity of the ignition time to small changes in temperature as:

$$\psi(T_0) = \frac{(\partial\tau/\partial T)_{T_0}}{\tau_0/T_0}. \tag{1.24}$$

In the preceding equation, a small change in temperature δT centered over a temperature T_0 results in a small change in ignition time $\delta\tau$ centered around an ignition time τ_0. The quantity ψ, which is plotted in Figure 1.8(b), measures the relative change in ignition time induced by a change in temperature. Figure 1.8(b) shows that in the band of temperatures between 950 to 1000 K, small changes in reactant temperatures (created by an acoustic wave, say) result in much larger changes in the mixture ignition time, which leads to significant oscillations in the ignition front position and heat release rate, potentially driving intrinsic thermoacoustic oscillations. Therefore, intrinsic thermoacoustic feedback can be quite important for autoignition fronts, given that small changes in temperature and pressure can significantly change the ignition front position and heat release rate by perturbing the ignition chemistry. In the context of Equation (1.22) applied to an autoignition front modeled by an $n-\tau$ transfer function, due to the high sensitivity of the ignition time of the autoigniting reactant mixture to

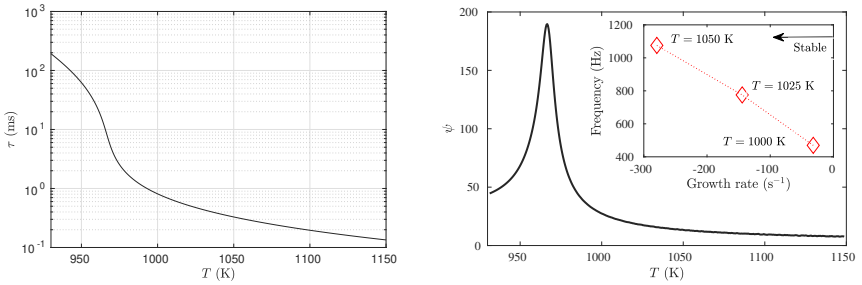

(a) **(b)**

Figure 1.8: (a) Variation of the ignition time of a hydrogen–air mixture with temperature. The equivalence ratio of the reactant mixture is 0.12, which corresponds to the mass fractions: $Y_{H_2} = 0.0028$, $Y_{O_2} = 0.1832$, $Y_{H_2O} = 0.0518$ and $Y_{N_2} = 0.7622$. (b) Sensitivity of the ignition time to small changes in temperature. The inset in (b) shows the frequency and growth rate of the ITA oscillations of the autoignition front with varying inlet reactant temperature. The mass fractions and the temperature range chosen is typical of reheat combustor conditions (Aditya et al., 2019), and the pressure is 1 atm.

temperature fluctuations, the critical gain could be easily attained, thus, favouring intrinsic thermoacoustic instability. The inset in Figure 1.8(b) plots the frequency and growth rate of the ITA oscillations associated with the autoignition front obtained from a reactive Euler equation computation where the mean temperature of the reactant mixture at the inlet is varied as a parameter. It can be clearly seen that the autoignition front tends to be progressively less-stable, in an intrinsic thermoacoustic sense, as the mean temperatures approach the maxima of the ψ vs T curve.

The acoustic–flow–flame interactions causing the ITA feedback in autoignition fronts is schematically depicted in Figure 1.9, which represents the signal flow graph of an active flame placed in an anechoic environment. This signal flow graph is inspired by similar ones constructed for propagation-stabilized flames by Emmert et al. (2015) and Bomberg et al. (2015). The configuration considered is a simplified one-dimensional combustor (Figure 1.7) with reactants entering the inlet at a sufficiently high temperature, resulting in autoignition at some location X_{ig0} downstream. The boundaries are perfectly non-reflecting and acoustic (f_1, g_2) and entropy (h_1) forcing are applied at the inlet (f_1, h_1) and the exit (g_2). The autoignition front, creating a jump in temperature, reflects and transmits these waves which appear as outgoing waves g_1 at the inlet and f_2, h_2 at the exit. In addition, the autoignition front responds unsteadily to the imposed forcing resulting in

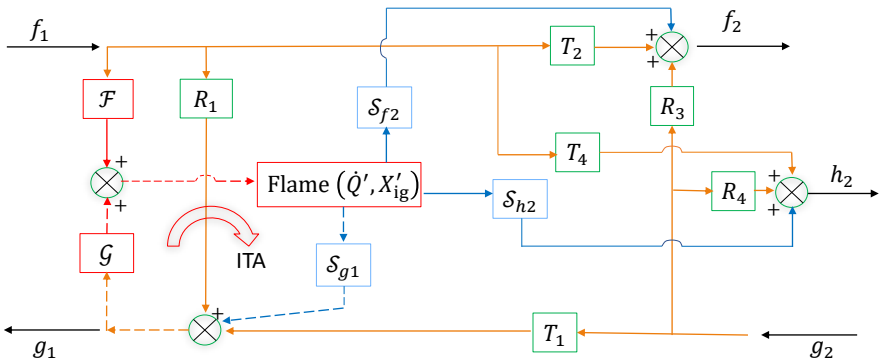

Figure 1.9: Signal flow graph of an active flame in an acoustic environment with no reflection from the boundaries. Each block represents a frequency dependent transfer function relating the output to the input. The intrinsic thermoacoustic feedback loop is represented by the dashed lines composed of: the upstream-traveling (g_1) wave modifying the flow, the flame response to the g_1 wave - $\mathcal{G}$, and the unsteady flame response generating a g_1 wave - $\mathcal{S}_{g1}$.

heat release rate ($\dot{Q}'$) and ignition front position (X'_{ig}) fluctuations, which act as sources of sound and also contribute to the outgoing acoustic and entropy waves.

Returning to Figure 1.9, it is to be noted that for the sake of compactness, the entropy wave imposed at the inlet is assumed to be zero. This does not change the dynamics of the ITA feedback, and is done purely to make the signal flow graph more presentable. Each of the blocks in Figure 1.9 represent a frequency dependent transfer function relating the output to the input. The outgoing waves are generated, partly, by the transmission and reflection of the imposed acoustic and entropy waves due to the change in acoustic impedance associated with the ignition front. For example, the g_1 wave is created by the reflection of the wave f_1 via the transfer function R_1 and transmission of the wave g_2 via the transfer function T_1. In addition to this mechanism, the waves f_1 and g_1 introduce temperature, pressure and velocity perturbations in the unburnt reactant mixture, modulating the ignition chemistry and the front kinematics, thereby creating harmonic heat release rate ($\dot{Q}'$) and flame position (X'_{ig}) fluctuations via the flame response functions $\mathcal{F}$ and $\mathcal{G}$. Finally, these heat release rate and front position fluctuations associated with an autoignition front also generate outgoing acoustic and entropy waves f_2, g_1 and h_2 via the transfer function $\mathcal{S}_{f2}, \mathcal{S}_{g1}$ and $\mathcal{S}_{h2}$. Thus, we have the intrinsic thermoacoustic feed-

back loop, shown in dashed lines in Figure 1.9, consisting of the g_1 wave modifying the flow and creating a flame response via $\mathcal{G}$ and the unsteady flame generating a g_1 wave via $\mathcal{S}_{g1}$.

To summarize, unstable thermoacoustic oscillations due to the ITA feedback, if manifested in a reheat stage of the sequential combustor, can lead to severe performance losses and impact the stable operation of the combustion system. Therefore, it is vital to get insight into these intrinsic thermoacoustic oscillations and develop modeling tools to enable prediction of these oscillations, which is the main aim of this work. Section 1.4 presents the current state of the art with respect to thermoacoustic modeling of reheat combustors, and Section 1.5 lists the main objectives of the present work.

1.4 Current state of the art

Prior studies related to thermoacoustic modeling of reheat combustors can be broadly subdivided into two categories: (i) detailed high-resolution CFD computations and experiments on reheat combustor configurations, and (ii) analytical physics based modeling studies on simplified reheat combustor configurations. First, the studies falling in category (i) are briefly discussed.

Bothien et al. (2019a) considered the autoignition-stabilized flame in a combustor geometry consisting of a backwards-facing step mimicking the Ansaldo Energia GT36 gas turbine (Pennell et al., 2017). Large eddy simulations (LES) were performed by forcing the autoignition front by velocity, pressure and temperature fluctuations at the domain boundaries. The full 3x3 transfer matrix relating the pressure, velocity and temperature fluctuations across the flame front was determined. A key result from this study was the importance of pressure and temperature fluctuations in describing the flame dynamics. The classical method of expressing the fluctuating heat release rate of the ignition front to the velocity fluctuations [Equation (1.6)] was not found to be sufficient, and the importance of temperature and pressure fluctuations was established. Additionally, the heat release response of the flame was found to be highly sensitive to temperature and pressure perturbations, while being relatively insensitive to velocity fluctuations.

Schulz and Noiray (2018) studied the response of an autoignition front stabilized in the second stage of a sequential combustor to temperature perturbations using LES computations. Their computations revealed that the

flame response was extremely sensitive to operating conditions and forcing amplitudes. Furthermore, they observed the formation of local autoignition kernels in the upstream mixing section, which convect downstream to the ignition front and result in a sudden increase in the heat release rate. This mechanism was identified as the primary reason for the nonlinear flame response behaviour of the autoignition front. In a separate study, Schulz et al. (2019) also showed the occurrence of thermoacoustic oscillations in a sequential combustor system. The thermoacoustic oscillations were attributed to the modulation of the inlet temperature at the reheat stage by the acoustic and convected entropy disturbances, which resulted in significant flame front oscillations.

Gruber et al. (2021) performed detailed and comprehensive DNS computations on autoignition fronts at laminar and turbulent conditions. They investigated the effect of varying temperature, pressure, velocity and equivalence ratio on the flame stability and the initial ignition process of hydrogen autoignition fronts. One key aspect to note in their work was the occurrence of self-excited thermoacoustic oscillations associated with the autoignition front at certain conditions. A hypothesis involving the modulation of the inlet temperature by the flame generated acoustic waves was proposed to be the reason for this unsteady flame behaviour.

Experiments performed at TU Munich by McClure et al. (2022) on a reheat combustor rig observed the occurrence of two high-frequency transverse thermoacoustic modes. The first mode, which happened at a frequency of 1600 Hz, was mainly attributed to the reactive shear layer modulation by the acoustically induced vortex shedding. Conversely, the second mode, which occurred at 3000 Hz, exhibited limit cycle oscillations and was driven by the modulation of the autoignition delay time by the acoustic perturbations.

The preceding studies demonstrated that even in simple laboratory scale burners, thermoacoustic instability resulting from autoignition front and acoustic wave interaction mechanisms can be very important, and therefore, should be understood and modeled in greater detail. This leads us to a discussion on studies which attempted to model and predict reheat flame dynamics.

Most of the studies performed to date on modeling of reheat flame dynamics focused on simplified reheat combustor geometries. Indeed, most of the studies that will be presented in the next paragraph focused on the one-dimensional configuration of Figure 1.7, which consists of a perfectly

premixed reactant mixture undergoing spontaneous ignition downstream. The beauty of this configuration is that it allows us to study the mechanism of flame-acoustic interactions without the complexity of hydrodynamic instabilities, equivalence ratio oscillations, multi-dimensional effects, and so on. In other words, the one-dimensional configuration allows us to understand the mechanisms by which acoustic waves modify the chemical kinetic processes involved in spontaneous ignition and result in unsteady flame response. In addition, detailed chemical kinetic schemes can be used to study the flame dynamics without much worry about computational costs.

The earliest attempt to model the response of an autoignition-stabilized flame to acoustic waves was performed by Zellhuber et al. (2014), who treated the one-dimensional flow in Figure 1.7 as a series of independently evolving fluid particles and derived an analytical expression for the heat release response of the autoignition front to acoustic pressure perturbations. Recently, Gant et al. (2020b) extended this model to entropy waves. Results in Gant et al. (2020b) and Gant et al. (2020a) showed that this model was able to predict, with excellent accuracy, the unsteady ignition front behaviour observed in 1D DNS computations, and was also able to predict, with good accuracy, the autoignition front transfer function in the full-scale GT26 engine. A key aspect to note in these models was that, an analytical approach was adopted and an exponential model for the ignition time variation with temperature was assumed, i.e., $\tau = \tau_0 e^{BT}$.

1.5 Objectives

The overarching goal of this thesis is to gain insight into thermoacoustic phenomena in reheat combustors with autoignition fronts and to develop predictive modeling tools to efficiently compute the linear thermoacoustic stability of reheat combustion systems. A variety of thermoacoustic interaction mechanisms as depicted in Figure 1.4 may, either individually or in combination, cause thermoacoustic instability in a reheat combustor. In this thesis, however, the focus is mainly placed on the intrinsic thermoacoustic interaction mechanism (see Figure 1.9). The aim, therefore, is to compute and model intrinsic thermoacoustic oscillations in reheat combustion systems. To address this overall objective, four objectives/goals are proposed to be achieved.

1. **To demonstrate the occurrence of intrinsic thermoacoustic oscillations in a reheat combustor and characterize the linear dynamics of**

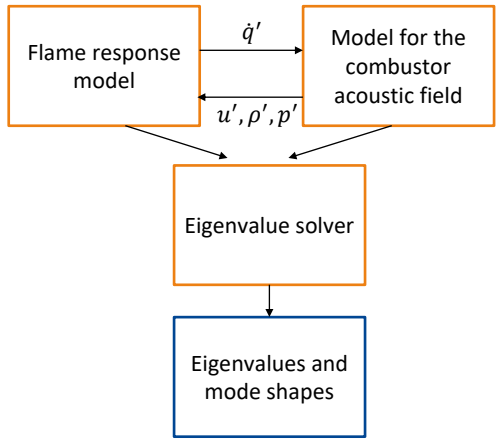

Figure 1.10: Schematic of a linear thermoacoustic stability analysis framework.

these oscillations.

In order to meet this objective, a compressible reactive Euler equation solver, which numerically solves the Euler equations in one-dimension with detailed chemistry is developed. Forced and unforced Euler equation computations are performed to demonstrate the occurrence of intrinsic thermoacoustic modes in a simplified 1D reheat combustor configuration (Figure 1.7).

This objective is met through Article 3 and Article 4. In Article 3, ITA oscillations are demonstrated by unforced flow computations, and the effect of diffusive effects on these oscillations are studied. In Article 4, the ITA oscillations are demonstrated and characterized by using forced flow computations.

2. **Develop a simplified framework to compute the unsteady response of autoignition-stabilized flames to acoustic and convective disturbances.**

   While detailed flow computations yield valuable insight into thermoacoustic phenomena in gas turbine combustors (Staffelbach et al., 2009), these computations are expensive and require many hours of compute time. A simplified linear stability analysis tool can be very useful to get quick and leading-order insight into the occurrence of thermoacoustic oscillations in a given combustor. Prediction of the linear stability of thermoacoustic oscillations requires two key ele-

ments (see Figure 1.10). First, a model for the flame response to acoustic and convective disturbances, and second, a model for the combustor acoustics. This objective aims to develop a flame response model. While separate analytical models have been developed in the past (Zellhuber et al., 2014; Gant et al., 2020b) to compute the flame dynamics of autoignition fronts, all these models assume an exponential dependence of ignition time with temperature, which is not strictly valid over the entire temperature range (see Figure 1.8a). Therefore, a numerical framework which is capable of predicting the flame response to one-dimensional disturbances would be useful in this regard. This framework could also be easily incorporated into linearized Navier–Stokes or Euler solvers to predict the thermoacoustic stability of the system.

Article 1 and Article 2 address this objective. A numerical framework based on Lagrangian particle tracking is developed to compute the flame response to acoustic and convective perturbations. This framework is also validated with one-dimensional DNS and three-dimensional LES computations. The Lagrangian framework is applied to a 1D configuration in Article 1 and to a two-dimensional backward-facing step configuration in Article 2

3. **Develop a simplified numerical framework to predict the acoustic field in reheat combustors with unsteady autoignition fronts.**

   A simplified model which accurately describes the acoustic field associated with unsteady autoignition fronts is very essential to predict the thermoacoustic stability of the system. Acoustic field associated with one-dimensional flame fronts have been described using the Rankine–Hugoniot jump conditions in the past (Dowling, 1995; Chen et al., 2016; Gant et al., 2022). However, such a model treats the flame as a discontinuous jump in the mean flow variables and the detailed spatial variations of the mean flow parameters is not taken into account. Additionally, both propagation and autoignition fronts harmonically change their position in response to acoustic and convective disturbances. This results in additional sources of sound due to gas property fluctuations, which cannot be trivially incorporated within a Rankine–Hugoniot framework. Therefore, it is essential to develop a more robust framework to compute the acoustic field generated by unsteady autoignition fronts.

   Article 3 addresses this objective. A time domain linearized Euler equation (LEE) solver is developed to compute the acoustic field as-

sociated with unsteady autoignition fronts. This LEE framework is validated by means of a comparison to forced DNS computations and is shown to compute the acoustic field in reheat combustors with good accuracy.

4. **Predict the linear intrinsic thermoacoustic modes in a reheat combustor configuration using the simplified frameworks and compare the predictions with detailed computations.**

   The simplified frameworks developed to meet the prior objectives are used to predict the linear stability of the ITA modes associated with an ignition front in the one-dimensional configuration. Article 4 addresses this objective, where the LEE framework developed to meet Objective 3 is used to compute the thermoacoustic eigenvalue of the ITA mode. These predictions are then compared with the Euler computations revealing a very good match.

Chapter 2

Computational and theoretical methods

This section describes the computational and theoretical methods used in this thesis to meet the objectives listed in Section 1.5. Most of the flow computations in this work are performed in an Euler equation framework, which is described in Section 2.1. An analytical expression of the dispersion relation governing the linear dynamics of the ITA oscillations is derived in Section 2.2, based on which predictions of the linear stability of the ITA modes are performed. The simplified frameworks for the flame response prediction and the acoustic field computation are described in Sections 2.3 and 2.4, respectively.

2.1 Flow solver: Euler equation framework

The geometrical configuration considered for all flow computations reported in this thesis is the simplified one-dimensional combustor configuration of Figure 1.7. This configuration is chosen, since the aim is to study the interaction between acoustic waves and the autoignition front, i.e., how does the acoustic wave modulate the autoignition chemistry and produce a self-sustained flame oscillation. In this configuration, the time scales of the advective and chemical processes are much smaller than the viscous time scale. Therefore, all computations are performed in an inviscid framework. Comparison of the Euler and Navier–Stokes computations of autoignition fronts presented in Articles 3 and 4, revealed very negligible differences.

The Euler equations for an inviscid reacting flow in one-dimension can be

written as (Poinsot and Veynante, 2005)

$$\begin{gathered}
\frac{\partial \rho}{\partial t} + \rho \frac{\partial u}{\partial x} + u \frac{\partial \rho}{\partial x} = 0, \\
\frac{\partial u}{\partial t} + u \frac{\partial u}{\partial x} + \frac{1}{\rho} \frac{\partial p}{\partial x} = 0, \\
\frac{\partial p}{\partial t} + u \frac{\partial p}{\partial x} - \gamma \rho T \frac{\partial R}{\partial t} - \gamma \rho u T \frac{\partial R}{\partial x} + \gamma p \frac{\partial u}{\partial x} = -(\gamma - 1) \sum_{i=1}^{n} h_i \mathrm{MW}_i \dot{\omega}_i, \\
\frac{\partial Y_i}{\partial t} + u \frac{\partial Y_i}{\partial x} = \frac{\mathrm{MW}_i \dot{\omega}_i}{\rho},
\end{gathered} \tag{2.1}$$

where ρ, u, p, Y_i denote the primitive variables density, velocity, pressure and species mass fraction, respectively. The specific gas constant of the mixture, temperature and species molecular weight are denoted by R, T and MW_i. The subscript 'i' denotes the species number, and $\dot{\omega}_i$ denotes the production rate of the i^{th} species. In writing the above equations, body forces are neglected and ideal gas behaviour is assumed.

Before discussing the numerical techniques to solve the above set of equations, the boundary condition formulation is presented. The method of characteristics is used to impose the boundary conditions for this flow. This procedure expresses the Euler equations at the boundary points in terms of the characteristic waves propagating in and out of the domain. Information about the boundary conditions and the mean flow quantities to be imposed are communicated to the flow by specifying the incoming characteristics.

2.1.1 Boundary condition implementation

The Euler equations (2.1) at the boundary points are first written in compact form as

$$\frac{\partial \mathbf{U}}{\partial t} + \mathbf{A} \frac{\partial \mathbf{U}}{\partial x} = \mathbf{S}, \tag{2.2}$$

where $\mathbf{U}$ is the vector containing the primitive variables: $[\rho, u, p, Y_i]^{\mathrm{T}}$, the second term represents all the terms involving the spatial derivatives, and $\mathbf{S}$ is the vector of the source terms: $[0, 0, S_p, S_{Y_i}]^{\mathrm{T}}$ of the Euler equations. The

expanded form of Equation (2.2) reads

$$\frac{\partial}{\partial t}\begin{bmatrix}\rho\\ u\\ p\\ Y_i\end{bmatrix}+\begin{bmatrix}u & \rho & 0 & 0\\ 0 & u & 1/\rho & 0\\ 0 & \gamma p & u & 0\\ 0 & 0 & 0 & u\end{bmatrix}\begin{bmatrix}\frac{\partial \rho}{\partial x}\\ \frac{\partial u}{\partial x}\\ \frac{\partial p}{\partial x}\\ \frac{\partial Y_i}{\partial x}\end{bmatrix}=\begin{bmatrix}0\\ 0\\ S_p\\ S_{Y_i}\end{bmatrix}, \tag{2.3}$$

where the terms involving the temporal and spatial derivatives of the gas property (R) in the energy equation are neglected at the boundary points.

Equation (2.2) can be rewritten by employing a similarity transformation for the matrix $\mathbf{A}$ as

$$\frac{\partial \mathbf{U}}{\partial t}+\mathbf{R}\Lambda\mathbf{R}^{-1}\frac{\partial \mathbf{U}}{\partial x}=\mathbf{S} \implies \mathbf{R}^{-1}\frac{\partial \mathbf{U}}{\partial t}+\Lambda\mathbf{R}^{-1}\frac{\partial \mathbf{U}}{\partial x}=\mathbf{R}^{-1}\mathbf{S}. \tag{2.4}$$

The matrices listed in Equation (2.4) can be written as

$$\mathbf{R}^{-1}=\begin{bmatrix}0 & 1/2 & -1/(2\rho c) & 0\\ 1 & 0 & -1/(c^2) & 0\\ 0 & 1/2 & 1/(2\rho c) & 0\\ 0 & 0 & 0 & 1\end{bmatrix},\quad \Lambda=\begin{bmatrix}u-c & 0 & 0 & 0\\ 0 & u & 0 & 0\\ 0 & 0 & u+c & 0\\ 0 & 0 & 0 & u\end{bmatrix} \tag{2.5}$$

Equation (2.4) can now be written in expanded form as

$$\begin{aligned}
\left(\frac{\partial p}{\partial t} - \rho c \frac{\partial u}{\partial t}\right) + \underbrace{(u-c)\left(\frac{\partial p}{\partial x} - \rho c \frac{\partial u}{\partial x}\right)}_{\mathscr{L}_1} &= \underbrace{S_p}_{\mathscr{S}_1}, \\
\left(c^2 \frac{\partial \rho}{\partial t} - \frac{\partial p}{\partial t}\right) + \underbrace{u\left(c^2 \frac{\partial \rho}{\partial x} - \frac{\partial p}{\partial x}\right)}_{\mathscr{L}_2} &= \underbrace{-S_p}_{\mathscr{S}_2}, \\
\left(\frac{\partial p}{\partial t} + \rho c \frac{\partial u}{\partial t}\right) + \underbrace{(u+c)\left(\frac{\partial p}{\partial x} + \rho c \frac{\partial u}{\partial x}\right)}_{\mathscr{L}_5} &= \underbrace{S_p}_{\mathscr{S}_5}, \\
\frac{\partial Y_i}{\partial t} + \underbrace{u \frac{\partial Y_i}{\partial x}}_{\mathscr{L}_{Y_i}} &= \underbrace{S_{Y_i}}_{\mathscr{S}_{Y_i}}.
\end{aligned} \tag{2.6}$$

Under the variable transformation $\mathbf{R}^{-1} d\mathbf{U} = d\mathbf{W}$, Equation 2.4 reduces to a set of advection equations, which can be written compactly as

$$\frac{\partial \mathbf{W}}{\partial t} + \Lambda \frac{\partial \mathbf{W}}{\partial x} = \mathbf{R}^{-1}\mathbf{S}, \tag{2.7}$$

where $\mathbf{W}$ is the vector of characteristic variables, and Λ represents the velocities associated with these characteristics. Equation (2.6) shows that these characteristics are simply the acoustic and entropy waves propagating at speeds $u-c$, $u+c$ and u, respectively. The final characteristic is the convected wave which conveys information about the species mass fractions

Equation (2.7) is commonly written in the literature as (Poinsot and Lele, 1992; Sutherland and Kennedy, 2003)

$$\frac{\partial \mathscr{W}_j}{\partial t} + \mathscr{L}_j = \mathscr{S}_j, \tag{2.8}$$

where $\mathscr{W}_j$ are the elements of the vector $\mathbf{W}$ representing the characteristic variables, $\mathscr{L}_j$ are the characteristic wave amplitudes, and $\mathscr{S}_j$ are the source terms in the characteristic direction. The characteristic wave amplitudes $\mathscr{L}_j$'s are composed of the upstream-traveling acoustic wave ($\mathscr{L}_1$), the downstream-traveling acoustic wave ($\mathscr{L}_5$), the downstream traveling entropy wave ($\mathscr{L}_2$), and the downstream traveling convected wave ($\mathscr{L}_{Y_i}$),

which conveys information about the species mass fractions. The direction of propagation of the acoustic and entropy waves ($\mathscr{L}_1, \mathscr{L}_5$ and $\mathscr{L}_2$) are depicted in Figure 1.7 for a subsonic flow in the positive x-direction. At the inlet boundary, the acoustic and entropy waves $\mathscr{L}_5$ and $\mathscr{L}_2$, in addition to the convected wave $\mathscr{L}_{Y_i}$, enter the computational domain from the exterior, while the acoustic wave $\mathscr{L}_1$ travels from the interior of the computational domain towards the exterior. Similarly, at the exit boundary, the waves $\mathscr{L}_2, \mathscr{L}_5$ and $\mathscr{L}_{Y_i}$ leave the computational domain while the acoustic wave $\mathscr{L}_1$ enters it.

For the sake of convenient computational implementation, it is beneficial to recast Equation (2.6) as

$$\begin{aligned} \frac{\partial \rho}{\partial t} + \frac{1}{c^2}\left(\mathscr{L}_2 + \frac{1}{2}(\mathscr{L}_1 + \mathscr{L}_5)\right) &= 0, \\ \frac{\partial u}{\partial t} + \frac{1}{2\rho c}\left(\mathscr{L}_5 - \mathscr{L}_1\right) &= 0, \\ \frac{\partial p}{\partial t} + \frac{1}{2}\left(\mathscr{L}_1 + \mathscr{L}_5\right) &= S_p, \\ \frac{\partial Y_i}{\partial t} + \mathscr{L}_{Y_i} &= S_{Y_i}. \end{aligned} \tag{2.9}$$

Implementation of the boundary conditions effectively amounts to solving Equation (2.9) by specifying the wave amplitudes entering the computational domain and computing the wave amplitudes leaving the computational domain using the spatial derivative expressions in Equation (2.6) and the interior data. Many different types of boundary condition can be implemented for flows. The reader is referred to Thompson (1987, 1990) and Poinsot and Lele (1992) for more details. In this thesis, two types of flow computations are performed: (i) unforced flow computations with non-reflecting boundary conditions, and (ii) forced flow computations with non-reflecting boundary conditions. Fully non-reflecting boundary conditions are realized when the time rate of change of the characteristic variables entering the computational domain are zero (Hedstrom, 1979), i.e.,

$$\frac{\partial \mathscr{W}_j}{\partial t} = 0 \implies \mathscr{L}_j = \mathscr{S}_j, \tag{2.10}$$

for any wave $\mathscr{L}_j$ entering the computational domain.

The wave amplitudes imposed for unforced flow computations are given

first. At the inlet boundary

$$\begin{aligned}\mathscr{L}_5 &= S_p + \rho c\frac{\sigma c(1-M^2)}{l}(u-u_{01t}),\\ \mathscr{L}_2 &= -S_p + c^2\frac{\sigma c(1-M^2)}{l}(\rho-\rho_{01t}),\\ \mathscr{L}_{Y_i} &= S_{Y_i},\end{aligned} \tag{2.11}$$

and at the outlet boundary

$$\mathscr{L}_1 = S_p + \frac{\eta c(1-M^2)}{l}(p-p_{02t}). \tag{2.12}$$

In the above equations, c denotes the local speed of sound, l denotes the length of the combustor taken to be 0.3 m for all computations performed in this work, and M represents the local flow Mach number. The second term in the RHS of Equations (2.11) and (2.12) are relaxation terms which are imposed to ensure that the mean values of the primitive variables at the boundary points are close to the target values of inlet velocity (u_{01t}), inlet density (ρ_{01t}) and exit pressure (p_{02t}). These terms are added to ensure that the primitive variables at the boundary point do not drift away too much from the target values. The parameters σ and η control the degree of non-reflectiveness of the inlet and exit boundaries. Lower the value of σ and η, more non-reflective are the boundaries.

The wave amplitudes imposed for the forced flow computations are written next, following Polifke et al. (2006) and Daviller et al. (2019). Acoustic and entropy forcing are applied at the inlet boundary by specifying

$$\begin{aligned}\mathscr{L}_5 &= S_p + \Big\{-2\rho c\frac{\partial u_t}{\partial t} + K\rho c(u-u_{01t}-u_t-u_-)\Big\},\\ \mathscr{L}_2 &= -S_p + \Big\{-c^2\frac{\partial \rho_t}{\partial t} + Kc^2(\rho-\rho_{01t}-\rho_t-\rho_- - \rho_{\mathscr{L}_5})\Big\},\\ \mathscr{L}_{Y_i} &= S_{Y_i},\end{aligned} \tag{2.13}$$

and acoustic forcing is applied at the outlet boundary by specifying

$$\mathscr{L}_1 = S_p + \Big\{-2\frac{\partial p_t}{\partial t} + K(p-p_{02t}-p_t-p_+)\Big\}, \tag{2.14}$$

where the terms within the curly braces essentially impose the acoustic and entropy forcing at the boundaries, and the term involving the source term

is used to maintain the non-reflective nature of the boundaries (waves originating from the interior of the computational domain should leave the domain unaltered and unreflected). In Equations (2.13) and (2.14), p_t, u_t and ρ_t represent the target values of the pressure, velocity and density oscillations induced by the imposed disturbances $\mathscr{L}_1, \mathscr{L}_5$ and $\mathscr{L}_2$, respectively. K is a parameter representative of an inverse time constant given by $\sigma c(1 - M^2)/l$, where a constant value of 0.5 is used for σ. It is important to note that p_t, u_t and ρ_t only represent the fluctuating quantities associated with the incoming waves and not the fluctuating values of the primitive variables themselves at the boundary points. The pressure fluctuations at the exit boundary, for example, will be the sum of p_t and the pressure fluctuation (p_+) induced by the downstream traveling acoustic wave $\mathscr{L}_5$. Similarly, the velocity perturbations at the inlet boundary will be the sum of u_t and the velocity fluctuation (u_-) imposed by the upstream-traveling acoustic wave $\mathscr{L}_1$.

In Equations (2.13) and (2.14), the flow perturbations induced by the acoustic waves traveling from the interior of the computational domain towards the boundaries are determined from a simple time integration as follows (Daviller et al., 2019)

$$\begin{aligned} u_- &= \int_0^t \frac{1}{2\rho c}\mathscr{L}_1(0,t)dt, \\ \rho_- &= -\int_0^t \frac{1}{2c^2}\mathscr{L}_1(0,t)dt, \\ p_+ &= -\frac{1}{2}\int_0^t \mathscr{L}_5(l,t)dt, \\ \rho_{L5} &= -\int_0^t \frac{1}{2c^2}\mathscr{L}_5(0,t)dt. \end{aligned} \tag{2.15}$$

Special care should be taken when performing the numerical integration in Equation (2.15). This is because, the wave amplitudes traveling from the interior of the computational towards the boundaries [$\mathscr{L}_1(0,t)$ and $\mathscr{L}_5(l,t)$] are typically computed from the spatial derivative expressions in Equation (2.6) and can sometimes have non-zero mean values which are small but finite. These non-zero mean values of the wave amplitudes are not physical and are numerically induced. When numerically performing the integration in Equation (2.15), these non-zero mean values cause a drift in the quantities u_-, ρ_- and p_+, eventually resulting in a drift in the primitive

variables at long times. To avoid this problem, the quantities computed in Equation (2.15) are filtered temporally using a high-pass filter (Daviller et al., 2019) to remove the spurious drift.

The transfer function (in the $z-$domain) of a digital Butterworth filter is given by

$$\frac{Y(z)}{X(z)} = \frac{c_0 + c_1 z^{-1} + c_2 z^{-2} + \cdots + c_N z^{-N}}{d_0 + d_1 z^{-1} + d_2 z^{-2} + \cdots + d_N z^{-N}}, \tag{2.16}$$

where $X(z)$ is the input signal, $Y(z)$ is the filtered signal, and N is the order of the filter.

Equation (2.16) can be rearranged to

$$\begin{aligned} Y(z) = \frac{c_0}{d_0}X(z) + \frac{c_1}{d_0}z^{-1}X(z) + \frac{c_2}{d_0}z^{-2}X(z) + \cdots + \frac{c_N}{d_0}z^{-N}X(z) \\ -\frac{d_1}{d_0}z^{-1}Y(z) - \frac{d_2}{d_0}z^{-2}Y(z) - \cdots - \frac{d_N}{d_0}z^{-N}Y(z), \end{aligned} \tag{2.17}$$

and can be converted to discrete time domain by taking the inverse z transform. The discrete time domain form of Equation (2.17) is

$$\begin{aligned} y[n] = \frac{c_0}{d_0}x[n] + \frac{c_1}{d_0}x[n-1] + \frac{c_2}{d_0}x[n-2] + \cdots + \frac{c_N}{d_0}x[n-N] \\ -\frac{d_1}{d_0}y[n-1] - \frac{d_2}{d_0}y[n-2] - \cdots - \frac{d_N}{d_0}y[n-N], \end{aligned} \tag{2.18}$$

where $x[n]$ denotes the value of the input signal at the discrete time instant n. Without loss of generality, d_0 can be put to 1 which gives

$$\begin{aligned} y[n] = c_0 x[n] + c_1 x[n-1] + c_2 x[n-2] + \cdots + c_N x[n-N] \\ -d_1 y[n-1] - d_2 y[n-2] - \cdots - d_N y[n-N]. \end{aligned} \tag{2.19}$$

A second order Butterworth filter with a cutoff frequency of $f_c = 0.1 f_{\text{forcing}}$ is used for all forced response computations in this work. The frequency domain characteristics of this filter is plotted in Figure 2.1, where it can be seen that the filter only cuts off the low frequency components and the gain and phase near the forcing frequency are close to 1 and 0 rad, respectively. The interior flow perturbations calculated using Equations (2.15) are filtered at each time step using Equation (2.19) to eliminate the spurious low-frequency drift.

Therefore, the Euler equations at the interior points [Equation (2.1)] together with the boundary conditions [Equation (2.9)], along with the wave

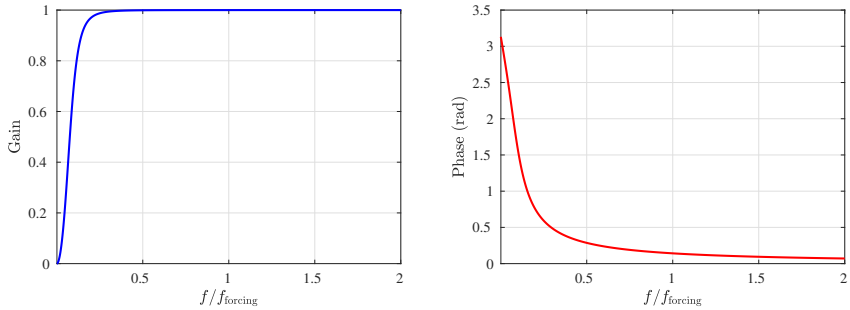

(a) **(b)**

Figure 2.1: (a) Gain and (b) phase characteristics of the high pass filter used for all the forced flow computations in this work.

amplitude expressions [Equations (2.11) and (2.12) or Equations (2.13) and (2.14)], and the interior flow perturbations [Equation (2.15)] are solved numerically to determine the evolution of the reacting flow in time. The numerical method used to solve these equations is presented next.

2.1.2 Numerical method

The main objective of the flow computations performed in this work is to understand the interactions between the acoustic perturbations and the autoignition front. Therefore, the numerical scheme that we employ should both capture the propagation of acoustic waves and handle the rapid spatial variations in the flow quantities due to combustion. Finite volume schemes are highly effective in capturing rapid variations in flow quantities caused, for example, by flames or shocks (LeVeque, 2002). However, these schemes are highly dissipative and do not capture the propagation of acoustic waves with high accuracy. Finite difference schemes, on the contrary, are very effective in capturing the propagation of acoustic waves but give rise to numerical instabilities when used to compute flames and shock waves (Tam, 2012). These numerical instabilities arise in the computed solution in the form of high wave number oscillations, which eventually contaminate the entire solution. However, previous research on these spurious high wave number oscillations have shown that they can be avoided with proper application of a spatial filter (Kennedy and Carpenter, 1994), or by adding artificial damping terms to the discretized form of the equations (Tam, 2012). Therefore, for its effectiveness in computing wave propagation problems and for its ease of computational implementation, we chose a finite difference scheme for the flow solver.

The dispersion relation preserving scheme originally proposed by Tam et al. (1993) is used in this work. The scheme was initially designed for computational aeroacoustics problems, and is fourth-order accurate in the spatial dimension and second-order accurate in time. The spatial derivative of any arbitrary function (f) at an interior point can be written as

$$\frac{\partial f}{\partial x} = \frac{1}{\Delta x} \sum_{j=-3}^{3} a_j f(x + j\Delta x), \tag{2.20}$$

where the coefficients of the scheme are listed in Table 2.1. Before employing this numerical scheme for the flow computations, it is first important to understand the characteristics of the scheme in wave number space. In other words, it is important to understand how well the scheme computes the derivative of a wave characterized by a spatial wave number. A few steps of this process, also referred to as Fourier analysis (Gustafsson, 2007), is illustrated below.

Table 2.1: Coefficients of the spatial discretization scheme at an interior point

Scheme coefficient	Value
a_0	0.0
$a_1 = -a_{-1}$	0.79926643
$a_2 = -a_{-2}$	−0.18941314
$a_3 = -a_{-3}$	0.02651995

We assume that the arbitrary function in Equation (2.20) takes the form of a wave $f(x) = \widetilde{f}e^{ikx}$, where k is the spatial wavenumber ($= 2\pi/\lambda$) characterising the wave. The analytical expression for the first-order spatial derivative can be written as

$$\frac{df}{dx} = ik\widetilde{f}e^{ikx}. \tag{2.21}$$

The continuous variable x can be converted to discrete form using $x_j = j\Delta x$, where j are the set of positive integers, and Δx is the constant grid spacing. Therefore, the exact value of the spatial derivative of the function f at the grid point x_j is

$$\left.\frac{df}{dx}\right|_{x=x_j} = ik\widetilde{f}e^{ik(j\Delta x)}. \tag{2.22}$$

The approximate value of the spatial derivative, computed from the finite-difference stencil, can be analytically written using Equation (2.20) as

$$\left.\frac{df}{dx}\right|_{x=x_j}^{\text{num}} = \frac{1}{\Delta x}\Big(a_{-3}\widetilde{f}e^{ik\Delta x(j-3)} + a_{-2}\widetilde{f}e^{ik\Delta x(j-2)} + a_{-1}\widetilde{f}e^{ik\Delta x(j-1)} + a_0\widetilde{f}e^{ik\Delta x(j)} + a_1\widetilde{f}e^{ik\Delta x(j+1)} + a_2\widetilde{f}e^{ik\Delta x(j+2)} + a_3\widetilde{f}e^{ik\Delta x(j+3)}\Big). \tag{2.23}$$

The preceding equation can be simplified to

$$\left.\frac{df}{dx}\right|_{x=x_j}^{\text{num}} = \frac{1}{\Delta x}\widetilde{f}e^{ik(j\Delta x)}\Big(a_{-3}e^{-3ik\Delta x} + a_{-2}e^{-2ik\Delta x} + a_{-1}e^{-ik\Delta x} + a_0 + a_1e^{ik\Delta x} + a_2e^{2ik\Delta x} + a_3e^{3ik\Delta x}\Big). \tag{2.24}$$

We can now express the numerical derivative expression in the form of Equation (2.22) as

$$\left.\frac{df}{dx}\right|_{x=x_j}^{\text{num}} = i\overline{k}\widetilde{f}e^{ik(j\Delta x)}, \tag{2.25}$$

where $\overline{k}$ is the modified wave number given by

$$\overline{k} = \frac{1}{i\Delta x}\Big(a_{-3}e^{-3ik\Delta x} + a_{-2}e^{-2ik\Delta x} + a_{-1}e^{-ik\Delta x} + a_0 + a_1e^{ik\Delta x} + a_2e^{2ik\Delta x} + a_3e^{3ik\Delta x}\Big). \tag{2.26}$$

The modified wave number can now be written in non-dimensional form as

$$\overline{k}\Delta x = \frac{1}{i}\Big(a_{-3}e^{-3ik\Delta x} + a_{-2}e^{-2ik\Delta x} + a_{-1}e^{-ik\Delta x} + a_0 + a_1e^{ik\Delta x} + a_2e^{2ik\Delta x} + a_3e^{3ik\Delta x}\Big). \tag{2.27}$$

The variation of the non-dimensional modified wave number for the DRP scheme is plotted in Figure 2.2. The x-axis is in the range $[0, \pi]$, since the lowest wavelength that can be captured in a grid with a spatial resolution of Δx is $2\Delta x$. The ideal finite difference scheme is expected to have the behavior $\overline{k}\Delta x = k\Delta x$ over a significant range of wave numbers. The DRP scheme exhibits this nature over the range of small wave numbers (long waves), but fails to capture the correct wave propagation for short waves. However, the DRP scheme performs exceptionally well in comparison to the classical second-order central scheme.

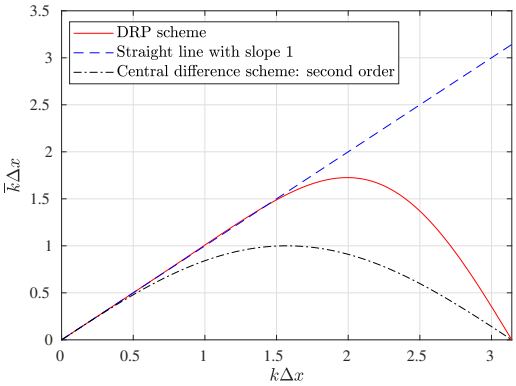

Figure 2.2: Modified wave number for the DRP scheme.

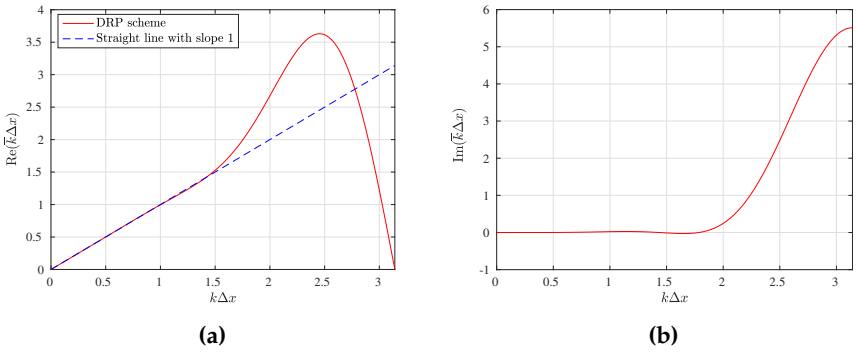

(a) **(b)**

Figure 2.3: Modified wave number for the boundary stencils of the DRP scheme.

At the boundary points of the computational domain, one-sided seven point stencils are used to approximate the derivatives. The coefficients of these stencils are given in Tam (2012) and are not repeated here. As an example, the approximation of the derivative at the first grid point can be written as

$$\left.\frac{df}{dx}\right|_{x=x_j}^{\text{bdy}} = \frac{1}{\Delta x}\left(a_0 f_j + a_1 f_{j+1} + a_2 f_{j+2} + a_3 f_{j+3} + a_4 f_{j+4} + a_5 f_{j+5} + a_6 f_{j+6}\right), \quad (2.28)$$

where $j = 0$ for the first grid point. The modified wave number for the boundary stencil is plotted in Figure 2.3. Unlike the modified wavenumber of the symmetric interior stencil, which is purely real (Figure 2.2), the boundary stencil also has an imaginary part. However, longitudinal combustion instabilities are usually characterized by long waves. In this regime, the imaginary part of the boundary stencil is close to zero and the real part is equal to $k\Delta x$, as desired.

For marching the governing equations in time, the following multi-level time stepping scheme proposed by Tam et al. (1993) is used.

$$\mathbf{U}^{n+1} = \mathbf{U}^n + \Delta t \sum_{j=0}^{3} b_j \left(\frac{\partial \mathbf{U}}{\partial t}\right)^{n-j}, \quad (2.29)$$

where $\mathbf{U}$ is the vector of the primitive variables, the superscript $n - j$ denotes the time level, and b_j are the coefficients of the time-stepping scheme, which are listed in Table 2.2. The quantity $\partial\mathbf{U}/\partial t$ at any time level is obtained from the governing equations and boundary conditions, and is composed of the terms involving spatial derivatives and source terms.

Table 2.2: Coefficients of the time-stepping scheme

Scheme coefficient	Value
b_0	2.3025580888383
b_1	−2.4910075998482
b_2	1.5743409331815
b_3	−0.3858914221716

2.1.3 Spatial filtering

In well resolved computations, numerical errors are mainly introduced at high wave numbers. This is apparent from Figure 2.2, where it is observed that the derivative operator has no resolution at $k\Delta x = \pi$. Nonlinear interactions between these unresolved waves generates high wave number information, which eventually contaminates the entire solution (Kennedy and Carpenter, 1994). From the personal experience of the author, numerically induced spurious (high wave number) oscillation is probably the worst nightmare of the CFD solver developer. During the course of the computation, grid to grid oscillations appear, seemingly out of nowhere, and in just a matter of a few hundred time steps contaminates and ruins the computed solutions.

Kennedy and Carpenter (1994) propose an ingenious method to remove these high wave number components from the solution. The analysis is performed in the wave number space. The idea proposed by Kennedy and Carpenter (1994) is to multiply the computed solutions every few time steps by a quantity, which, when transformed to the wave number space, should cutoff all high wave number components of the solution and retain only those components at low wave numbers.

The proposed filter functions have the form

$$F(\xi) = 1 - \sin^{2n}\left(\frac{\xi}{2}\right), \tag{2.30}$$

where $\xi = k\Delta x$ is the Fourier variable (non-dimensional wave number), and F is the filter function. The filter function F is plotted in Figure 2.4 for varying values of n from 1 to 5. As desired, the value of the function is 1 for low wave numbers and goes to zero at higher wave numbers. Additionally, at higher values of n, the filter preserves the information over a longer range of low wave numbers.

Filters with the mathematical form given by Equation (2.30) in Fourier space can be realized in physical space by performing the following operation on the discrete function f_j

$$\mathbf{D}\{f_j\} = \Upsilon f_j + a(f_{j+1} + f_{j-1}) + b(f_{j+2} + f_{j-2}) + c(f_{j+3} + f_{j-3}) + \cdots . \tag{2.31}$$

The above operation in the physical space on the function $f_j = \widetilde{f} e^{ik(j\Delta x)}$ can be transformed to wave number space resulting in a multiplicative factor

$$\Upsilon + 2a\cos(\xi) + 2b\cos(2\xi) + 2c\cos(3\xi) + \cdots . \tag{2.32}$$

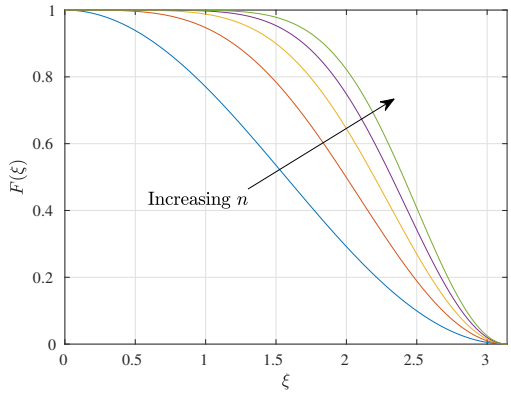

Figure 2.4: Transfer function of the spatial filter of Equation (2.30) for varying n.

When the coefficients $a, b, c, \cdots$, in the above equation are taken to be the second-order accurate stencils of the derivative $-\partial^{2n} f/\partial x^{2n}$, the mathematical form of Equation (2.30) will be recovered. This is best illustrated by examples. Let us first consider the case where $n = 1$. The coefficients for the second-order accurate versions of the second derivative operator are: $\Upsilon = 2, a = -1$. Substituting these values in Equation (2.32) yields

$$2 - 2\cos(\xi) = 4\sin^2\left(\frac{\xi}{2}\right) \tag{2.33}$$

Similarly, when $n = 2$, Equation (2.32) simplifies to

$$-6 + 8\cos(\xi) - 2\cos(2\xi). \tag{2.34}$$

The above expression can be successively simplified as

$$\begin{aligned} -6 + 8\cos(\xi) - 2\cos(2\xi) &= -6 + 8\cos(\xi) - 2\left(1 - 8\sin^2\left(\frac{\xi}{2}\right)\cos^2\left(\frac{\xi}{2}\right)\right) \\ &= -8(1 - \cos(\xi)) + 16\sin^2\left(\frac{\xi}{2}\right)\cos^2\left(\frac{\xi}{2}\right) \\ &= -16\sin^2\left(\frac{\xi}{2}\right) + 16\sin^2\left(\frac{\xi}{2}\right)\cos^2\left(\frac{\xi}{2}\right) \\ &= -16\sin^4\left(\frac{\xi}{2}\right). \end{aligned} \tag{2.35}$$

Therefore, application of the operator **D** for any value of n in physical space translates to multiplication by the quantity

$$(-1)^{n+1}\left[2\sin\left(\frac{\xi}{2}\right)\right]^{2n} \tag{2.36}$$

in the wave number (Fourier) space. Thus, filter function of the form of Equation (2.30) can be accomplished by performing the following operation in physical space

$$\mathbf{U}^{\text{filt}} = (1 + \alpha\mathbf{D})\mathbf{U}, \tag{2.37}$$

where α is given by $(-1)^n(2)^{-2n}$, **U** is the vector of primitive variables which need to be filtered, and $\mathbf{U}^{\text{filt}}$ is the filtered solution vector. Boundary stencils for the filter are developed by taking low-order accurate versions of the second derivative operator. These stencils can be found in Kennedy and Carpenter (1994).

2.1.4 Chemical kinetics

The final, and probably one of the most important, component of the CFD solver is presented in this sub-section: chemistry routines. These are the sub programs of the code which compute the source terms of the species mass balance and energy equations. The source terms are composed of the species production rates, which are computed for each species from the chemical mechanism. Any generic chemical mechanism can be written in compact form as (Turns et al., 1996)

$$\sum_{j=1}^{N} \nu'_{ij} X_j \rightleftharpoons \sum_{j=1}^{N} \nu''_{ij} X_j \quad \text{for} \quad i = 1, 2, \cdots, L, \tag{2.38}$$

where X_j symbolically represents the j^{th} species, N is the number of species, L is the number of reactions, ν'_{ij} are the stoichiometric coefficients of the reactants, and ν''_{ij} are the stoichiometric coefficients of the products.

Considering, for just the purpose of illustration, the incomplete hydrogen-oxygen reaction mechanism in Turns et al. (1996):

$$\mathrm{H_2 + O_2 \rightleftharpoons HO_2 + H} \tag{2.39}$$

$$\mathrm{H + O_2 \rightleftharpoons OH + O} \tag{2.40}$$

$$\mathrm{OH + H_2 \rightleftharpoons H_2O + H} \tag{2.41}$$

$$\mathrm{H + O_2 + M \rightleftharpoons HO_2 + M} \tag{2.42}$$

Assuming the species order is: O_2, H_2, H_2O, HO_2, O, H, OH, M, the matrices ν'_{ij} and ν''_{ij} can be written as

$$\nu'_{ij} = \begin{bmatrix} 1 & 1 & 0 & 0 & 0 & 0 & 0 & 0 \\ 1 & 0 & 0 & 0 & 0 & 1 & 0 & 0 \\ 0 & 1 & 0 & 0 & 0 & 0 & 1 & 0 \\ 1 & 0 & 0 & 0 & 0 & 1 & 0 & 1 \end{bmatrix}, \tag{2.43}$$

$$\nu''_{ij} = \begin{bmatrix} 0 & 0 & 0 & 1 & 0 & 1 & 0 & 0 \\ 0 & 0 & 0 & 0 & 1 & 0 & 1 & 0 \\ 0 & 0 & 1 & 0 & 0 & 1 & 0 & 0 \\ 0 & 0 & 0 & 1 & 0 & 0 & 0 & 1 \end{bmatrix}. \tag{2.44}$$

The production rate of the species j is given by

$$\dot{\omega}_j = \sum_{i=1}^{L} \nu_{ij} q_i, \text{ for } j = 1, 2, \cdots, N, \tag{2.45}$$

where

$$\nu_{ij} = (\nu''_{ij} - \nu'_{ij}), \tag{2.46}$$

and the rate of progress of the reaction is given by

$$q_i = k_{fi} \prod_{j=1}^{N} [X_j]^{\nu'_{ij}} - k_{ri} \prod_{j=1}^{N} [X_j]^{\nu''_{ij}}, \tag{2.47}$$

where k_{fi} and k_{ri} are the rate constants of the forward and reverse reactions, $[X_j]$ represents the molar concentration of the species j, given by $\rho Y_j / \mathrm{MW}_j$. The forward and reverse reaction rate constants are obtained from the chemical reaction mechanism. In all flow computations performed in this work, the chemical mechanism proposed by Li et al. (2004) for hydrogen-air combustion is used. This mechanism is composed of 9 species which participate in 21 reactions. Three types of chemical reactions are present in this mechanism, each characterized by a different method to compute the rate constants (Goodwin et al., 2022), which are presented next.

1. **Elementary reaction**: An elementary reaction is one of the basic types of reactions with pressure independent rate coefficient. Consider, for example, the elementary reaction

$$\mathrm{A} + \mathrm{B} \rightleftharpoons \mathrm{C} + \mathrm{D}. \tag{2.48}$$

The forward rate constant for this reaction is given by

$$k_f = AT^b e^{-E_a/R_u T}, \tag{2.49}$$

where A is the pre-exponential factor, b is the temperature exponent, E_a is the activation energy associated with the reaction, T is the temperature, and R_u is the universal gas constant.

2. **Three-body reaction**: A three-body reaction takes the form

$$\mathrm{A} + \mathrm{B} + \mathrm{M} \rightleftharpoons \mathrm{AB} + \mathrm{M}, \tag{2.50}$$

where M is a collision partner that takes away the excess energy to stabilize the AB molecule in the forward direction or supplies energy to break the bond in AB to form A and B in the reverse direction. All the species in the chemical reaction need not be equally efficient as the collision partner. Therefore, a third body efficiency is associated with each species. For a three-body reaction, the forward rate constant is calculated by multiplying Equation (2.49) by the factor [M] which is defined as

$$[\mathrm{M}] = \sum_k \varepsilon_k C_k, \tag{2.51}$$

where C_k is the concentration of the species k, and ε_k is the third-body efficiency factor, which is taken to be 1.0 unless otherwise specified in the reaction mechanism.

3. **Falloff reaction**: A falloff reaction has a rate that is first order in [M] at low pressure, but becomes zero order in [M] at higher pressures. The forward rate constant for such a reaction can be written in the form

$$k_f(T, [\mathrm{M}]) = \frac{k_0[\mathrm{M}]}{1 + k_0[\mathrm{M}]/k_\infty}. \tag{2.52}$$

At low pressures (low concentrations of third body molecule), k_f approaches $k_0[\mathrm{M}]$. At high pressures (high concentrations of third body

molecule), k_f approaches k_∞. A non-dimensional pressure can be defined as $P_r = k_0[\mathrm{M}]/k_\infty$, and Equation (2.52) can be modified to

$$k_f(T, [\mathrm{M}]) = k_\infty \frac{P_r}{1 + P_r}. \tag{2.53}$$

Some reactions also exhibit more complex forms of dependence of the forward rate constant on the reduced pressure. These can be accounted for by multiplying the rate expression in Equation (2.53) by a falloff function $F(T, P_r)$. A Troe falloff function (Goodwin et al., 2022) is used for all falloff reactions in the chemical mechanism used in this work.

The reverse reaction rates are calculated from the forward reaction rates by assuming equilibrium and using the Gibbs free energy change (ΔG^0_T) for that reaction (Turns et al., 1996). If we consider a generic single step reaction

$$\mathrm{aA} + \mathrm{bB} \rightleftharpoons \mathrm{cC} + \mathrm{dD}. \tag{2.54}$$

At equilibrium, the rate of formation of any species (for example, A) is zero. This gives

$$-a\left(k_f[\mathrm{A}]^a[\mathrm{B}]^b - k_r[\mathrm{C}]^c[\mathrm{D}]^d\right) = 0, \tag{2.55}$$

which can be simplified to give a relation involving the forward and reverse rate constants:

$$k_r = k_f \frac{[\mathrm{A}]^a[\mathrm{B}]^b}{[\mathrm{C}]^c[\mathrm{D}]^d} = \frac{k_f}{K_c}, \tag{2.56}$$

where K_c is the equilibrium constant based on concentrations. K_c can be related to K_p, the equilibrium constant based on partial pressures, using the relation

$$K_c = K_p \left(\frac{P_0}{R_u T}\right)^{\sum \nu_i'' - \sum \nu_i'}, \tag{2.57}$$

where P_0 is taken to be 1 atm, and K_p is given by

$$K_p = \exp\left(-\Delta G^0_T / R_u T\right). \tag{2.58}$$

The Gibbs free energy change for the reaction (2.54) is given by

$$\Delta G^0_T = \left(d g^0_d(T) + c g^0_c(T) - b g^0_b(T) - a g^0_a(T)\right). \tag{2.59}$$

The Gibbs free energy for each species as functions of temperature are given by the NASA seven coefficient polynomial fits (Burcat and Ruscic, 2005):

$$\frac{g_T^0}{R_u T} = a_1(1 - \ln T) - \frac{a_2 T}{2} - \frac{a_3 T^2}{6} - \frac{a_4 T^3}{12} - \frac{a_5 T^4}{20} + \frac{a_6}{T} - a_7. \tag{2.60}$$

In a similar manner, the specific heats and total enthalpies (sum of formation and sensible) of the species are also determined by Polynomial fits (Burcat and Ruscic, 2005) as

$$\frac{H_T}{RT} = a_1 + \frac{a_2 T}{2} + \frac{a_3 T^2}{3} + \frac{a_4 T^3}{4} + \frac{a_5 T^4}{5} + \frac{a_6}{T}, \tag{2.61}$$

$$\frac{C_p}{R} = a_1 + a_2 T + a_3 T^2 + a_4 T^3 + a_5 T^4. \tag{2.62}$$

2.2 Prediction of intrinsic thermoacoustic modes: theory

In this section, an analytical expression which will be used to predict the thermoacoustic eigenvalues of the intrinsic thermoacoustic feedback loop is presented. We consider the simple geometrical configuration of Figure 1.7, where an autoignition front is stabilized in the one-dimensional duct and forced by acoustic and entropy disturbances. As previously discussed in Section 1.3, the linear dynamics of the intrinsic thermoacoustic feedback, specifically the frequencies and growth rates of the oscillations, can be obtained from the poles of the scattering matrix (Hoeijmakers et al., 2014). Therefore, the aim of this section is to derive an expression for the poles of the scattering matrix associated with an autoignition front.

For the flow configuration in Figure 1.7, the scattering matrix can be written as

$$\begin{bmatrix} f_2 \\ g_1 \\ h_2 \end{bmatrix} = \begin{bmatrix} S_{11} & S_{12} & S_{13} \\ S_{21} & S_{22} & S_{23} \\ S_{31} & S_{32} & S_{33} \end{bmatrix} \begin{bmatrix} f_1 \\ g_2 \\ h_1 \end{bmatrix}, \tag{2.63}$$

where the mathematical expressions for the various characteristic waves are derived in Appendix A.

We start by writing expressions for each of the outgoing characteristics. The outgoing characteristics in the configuration of Figure 1.7 are created

by three distinct mechanisms: (i) transmission of the incoming characteristics by the temperature jump associated with the flame front, (ii) reflection of the incoming characteristics by the temperature jump associated with the flame front, and (iii) generation by the unsteady ignition front due to heat release rate and ignition front position perturbations. Mathematically, the above statement can be expressed as

$$\begin{bmatrix} f_2/p_0 \\ g_1/p_0 \\ h_2/p_0 \end{bmatrix} = \underbrace{\begin{bmatrix} T_2 & R_3 & T_3 \\ R_1 & T_1 & R_2 \\ T_4 & R_4 & T_5 \end{bmatrix}}_{\text{Transmission and reflection}} \begin{bmatrix} f_1/p_0 \\ g_2/p_0 \\ h_1/p_0 \end{bmatrix} + \underbrace{\begin{bmatrix} S_3 \\ S_1 \\ S_5 \end{bmatrix} \frac{\widetilde{\dot{Q}}}{\dot{Q}_0} + \begin{bmatrix} S_4 \\ S_2 \\ S_6 \end{bmatrix} \frac{\widetilde{X}_{\text{ig}}}{X_{\text{ig0}}}}_{\text{Generation by the ignition front}} , \tag{2.64}$$

where the R_i's and T_i's denote the frequency dependent functions which govern the reflection and transmission of the incoming characteristics to the outgoing characteristics by the ignition front. These terms are present even in the hypothetical case wherein the flame does not actively respond to the imposed disturbances ($\dot{Q}' = X'_{\text{ig}} = 0$). The frequency response functions S_i's govern the outgoing characteristics generated by the integrated heat release rate and ignition front position fluctuations, i.e., the sound/entropy generated by an unsteady ignition front. While integrated heat release rate fluctuations ($\dot{Q}'$) behaves as a monopole source of sound (Strahle, 1971), fluctuations in ignition front position (X'_{ig}) acts like an axially oriented acoustic dipole. Equation (2.64), in essence, simply states that the outgoing characteristics are a linear combination of transmission and reflection of the incoming waves and the generation by the unsteady ignition front. Of course, care should be taken when applying Equation (2.64) to combustor domains with complicated geometries. In such cases, additional terms due to, for example, acoustic reflection by solid walls can also show up.

It is important to realize that, as such, Equation (2.64) represents an open loop system where $\widetilde{\dot{Q}}$ and $\widetilde{X}_{\text{ig}}$ are treated as autonomous inputs, while in reality, they are dependent on the acoustic and entropy perturbations. Indeed, for autoignition fronts, $\widetilde{\dot{Q}}$ and $\widetilde{X}_{\text{ig}}$ intricately depend on how the various perturbations associated with an acoustic/entropy wave modify the ignition chemistry and the front kinematics and therefore, depend on the flow perturbations in a non-trivial manner. Closed loop dynamics of the ITA feedback can be obtained from Equation (2.64) when the heat release

rate and ignition front fluctuations associated with the autoignition front are related back to the acoustic and entropy perturbations via the flame transfer functions. For propagation-stabilized flames, it is common to write the integrated heat release rate fluctuations in terms of the velocity oscillations at some reference location upstream of the flame (McManus et al., 1993). This makes perfect sense because, as already pointed out before, propagating flames stabilized at low Mach numbers mainly respond to velocity oscillations induced by an acoustic wave. For autoignition fronts, on the other hand, it makes more sense to relate the flame response to the individual waves rather than to the fluctuations in primitive variables. This is because prior works (Gant et al., 2020b; Gopalakrishnan et al., 2021) have shown that acoustic and entropy waves modify the ignition chemistry differently and produce qualitatively different frequency responses in terms of the ignition length and integrated heat release rate fluctuations. Additionally, writing the heat release rate response in terms of velocity fluctuations does not take into account the influence of temperature disturbances induced by the entropy wave on the flame dynamics (Bothien et al., 2019a; Gant et al., 2020b).

Thus, the flame response written in terms of the characteristic waves for the integrated heat release rate reads

$$\frac{\widetilde{\dot{Q}}}{\dot{Q}_0} = F_1(s)\frac{f_1}{p_0} + F_2(s)\frac{g_1}{p_0} + F_3(s)\frac{h_1}{p_0}, \tag{2.65}$$

and for the ignition length

$$\frac{\widetilde{X}_{\mathrm{ig}}}{X_{\mathrm{ig0}}} = G_1(s)\frac{f_1}{p_0} + G_2(s)\frac{g_1}{p_0} + G_3(s)\frac{h_1}{p_0}. \tag{2.66}$$

In writing Equations (2.65) and (2.66), it is assumed that the autoignition front only responds to the fluctuations created by the characteristic waves upstream of the ignition front - f_1, g_1 and h_1. This is reasonable as it is these waves which modulate the autoignition chemistry and also introduce velocity oscillations upstream of the ignition front, creating fluctuations in the front position and the integrated heat release rate. In Equations (2.65) and (2.66), F_i represents the transfer function relating the heat release rate fluctuations to the characteristic waves, and G_i represents the transfer function relating the ignition length fluctuations to the characteristic waves.

Equation (2.64) is now modified to give insight into the dynamics of the ITA feedback by substituting Equations (2.65) and (2.66) for the flame re-

sponse. The second row in Equation (2.64), after this modification, reads

$$\frac{g_1}{p_0} = (R_1 + S_1F_1 + S_2G_1)\frac{f_1}{p_0} + (R_2 + S_1F_3 + S_2G_3)\frac{h_1}{p_0} + (T_1)\frac{g_2}{p_0} + (S_1F_2 + S_2G_2)\frac{g_1}{p_0}. \tag{2.67}$$

Equation (2.67) reveals that the term g_1/p_0 is present in both the LHS (response) and the RHS (excitation), suggesting that a closed loop feedback is set up by the g_1 wave. Further simplification of Equation (2.67) and comparison with the second row of the scattering matrix [Equation (2.63)] yields

$$\frac{g_1}{p_0} = \underbrace{\left(\frac{R_1 + S_1F_1 + S_2G_1}{1 - S_1F_2 - S_2G_2}\right)}_{S_{21}}\frac{f_1}{p_0} + \underbrace{\left(\frac{T_1}{1 - S_1F_2 - S_2G_2}\right)}_{S_{22}}\frac{g_2}{p_0} + \underbrace{\left(\frac{R_2 + S_1F_3 + S_2G_3}{1 - S_1F_2 - S_2G_2}\right)}_{S_{23}}\frac{h_1}{p_0}. \tag{2.68}$$

The first and third rows of the Equation set (2.64) can also be expanded by substituting Equations (2.65), (2.66) and (2.68) into them. The steps involved in this procedure are omitted and only the final expression is presented.

First row of Equation (2.64):

$$\frac{f_2}{p_0} = \underbrace{\Big((S_3F_1 + S_4G_1 + T_2) + (S_3F_2 + S_4G_2)S_{21}\Big)}_{S_{11}}\frac{f_1}{p_0} + \underbrace{\Big(R_3 + (S_3F_2 + S_4G_2)S_{22}\Big)}_{S_{12}}\frac{g_2}{p_0} + \underbrace{\Big((S_3F_3 + S_4G_3 + T_3) + (S_3F_2 + S_4G_2)S_{23}\Big)}_{S_{13}}\frac{h_1}{p_0}. \tag{2.69}$$

Third row of Equation (2.64):

$$\frac{h_2}{p_0} = \underbrace{\Big((S_5F_1 + S_6G_1 + T_4) + (S_5F_2 + S_6G_2)S_{21}\Big)}_{S_{31}}\frac{f_1}{p_0} + \underbrace{\Big(R_4 + (S_5F_2 + S_6G_2)S_{22}\Big)}_{S_{32}}\frac{g_2}{p_0} + \underbrace{\Big((S_5F_3 + S_6G_3 + T_5) + (S_5F_2 + S_6G_2)S_{23}\Big)}_{S_{33}}\frac{h_1}{p_0}. \tag{2.70}$$

Equations (2.69), (2.68) and (2.70) analytically express each row, and therefore each element, of the scattering matrix [Equation (2.63)] in terms of the

frequency response functions governing the flame dynamics (F_i's and G_i's), the sound and entropy generation by the unsteady ignition front (S_i's), and the reflection and transmission of acoustic and entropy waves by the ignition front (R_i's and T_i's). A vital aspect to notice in Equations (2.69), (2.68) and (2.70) is that all the terms of the scattering matrix have a common denominator, which is given by the expression $D(s) = 1 - S_1F_2 - S_2G_2$. When $D(s)$ goes close to zero, S_{21}, S_{22} and S_{23} reach high magnitudes, which results in significant amplifications of the g_1 wave. Additionally, also observe from Equations (2.69) and (2.70) that both f_2 and h_2 are linear combinations of terms involving S_{21}, S_{22} and S_{23}. Therefore, when $D(s)$ goes close to zero, significant amplifications of f_2 and h_2 are also expected due to the high magnitudes of the elements S_{21}, S_{22} and S_{23}. This suggests that the frequency dependent function $D(s) = 1 - S_1F_2 - S_2G_2$, can be factored out from the denominators of all the individual elements of the scattering matrix resulting in

$$\begin{bmatrix} f_2 \\ g_1 \\ h_2 \end{bmatrix} = \frac{1}{D(s)} \begin{bmatrix} S^*_{11} & S^*_{12} & S^*_{13} \\ S^*_{21} & S^*_{22} & S^*_{23} \\ S^*_{31} & S^*_{32} & S^*_{33} \end{bmatrix} \begin{bmatrix} f_1 \\ g_2 \\ h_1 \end{bmatrix}, \tag{2.71}$$

where the zeros of the dispersion relation $D(s)$ govern the oscillation frequencies and growth rates of the intrinsic thermoacoustic modes. Interestingly, $D(s)$ only involves the frequency dependent functions governing the thermal response of the ignition front to a g_1 wave (F_2 and G_2) and the generation of a g_1 wave by the unsteady ignition front (S_1 and S_2). This is to be expected as the ITA feedback mechanism, as depicted in Figure 1.9, only involves the g_1 wave and the associated thermal and acoustic responses that it consequently produces. The ITA feedback loop initially depicted in Figure 1.9 is schematically shown in terms of the relevant flame response and sound generation transfer functions in Figure 2.5.

To summarize, the prediction of the linear stability of the ITA oscillations associated with an autoignition front reduces to finding the complex valued quantity s satisfying the dispersion relation

$$D(s) = 0, \quad \text{where} \quad D(s) = 1 - S_1F_2 - S_2G_2. \tag{2.72}$$

Therefore, the aim of simplified models used to predict the linear stability of the ITA oscillations is to compute the transfer functions F_2, G_2 and S_1, S_2 accurately. In this thesis, we use a Lagrangian framework to compute the

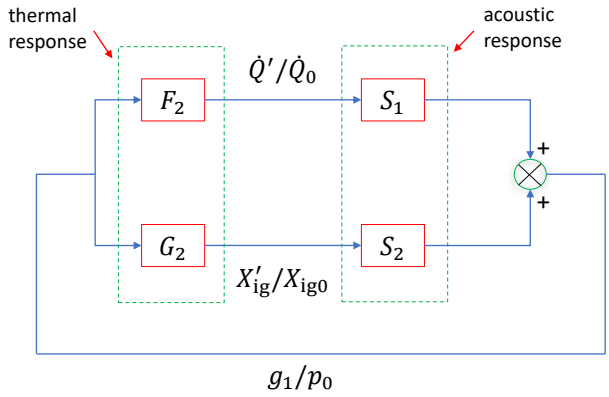

Figure 2.5: Intrinsic thermoacoustic feedback loop in terms of the flame response and sound generation transfer functions.

thermal response of the flame (discussed in Section 2.3), and a linearized Euler equation solver to compute the acoustic response of the flame (discussed in Section 2.4).

2.3 Lagrangian flame response framework

In this section, the Lagrangian flame response framework, which is used to predict the thermal response of the autoignition front to acoustic and convective disturbances is presented. This framework is formulated in this section for the one-dimensional flow configuration of Figure 1.7. However, extension to multiple dimensions is straightforward and is discussed in Article 2.

To compute the flame response to the imposed disturbances, the reacting flow is visualized as a series of non-interacting independently evolving fluid particles. We first consider discrete time instants

$$t_i = 0, \Delta t, 2\Delta t, \cdots, \mathcal{T},$$

where $\mathcal{T}$ is the time period of the imposed acoustic/convective disturbances, and Δt is the injection time interval. At each time instant t_i, a fluid particle is injected at the combustor inlet (see Figure 2.6). The evolution of each fluid particle in Lagrangian time t^* is then computed by time integrating the governing equations for each particle. It is important to note that t^* is a fictitious local time assigned to each particle for the purpose of tracking that particle. For any given particle, $t^* = 0$ at the instant this

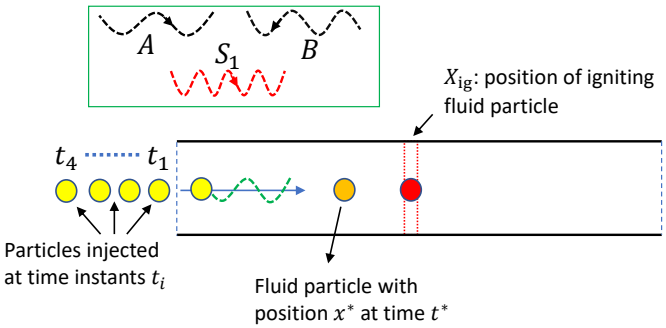

Figure 2.6: Schematic of the combustor geometry with the particle injection scheme used for the Lagrangian framework. The green box shows the acoustic and entropy perturbations

particle is injected at the combustor inlet. The time t^*, which can be visualized as a 'clock' attached to a fluid particle which starts ticking the moment the particle is injected, is different from the physical global time t. If t_i is the time at which a particle is injected at the combustor inlet, the relation between global time and particle time is given by $t = t_i + t^*$. The global flame response is computed by stitching together the individual particle evolution.

In the following, the method to compute the Lagrangian evolution of temperature of a fluid particle injected at the combustor inlet at time t_i is presented. The following process has to be repeated for different particles injected at various time instants to get the overall flame response. The change in temperature (ΔT) of a fluid particle over a small time interval of Δt^* is a combination of the temperature change due to chemical reactions (ΔT_c) and the temperature change due to acoustic and entropy disturbances (ΔT_d). Thus, we can write

$$\Delta T = \Delta T_c + \Delta T_d. \tag{2.73}$$

The above equation can be written in terms of derivatives by taking the limit $\Delta t^* \to 0$:

$$\frac{DT}{Dt^*} = \frac{DT_c}{Dt^*} + \frac{DT_d}{Dt^*}. \tag{2.74}$$

The first term in the RHS of the above equation, which is the time rate of change of temperature of a fluid particle due to chemical reactions, is given by the Lagrangian form of the energy equation (Poinsot and Veyn-

ante, 2005).

$$\frac{DT_c}{Dt^*} = -\frac{1}{\rho C_p}\sum_{i=1}^{n} h_i \mathrm{MW}_i \dot{\omega}_i, \tag{2.75}$$

where the notation convention adopted is the same as in Section 2.1. In writing the above equation, diffusive terms (viscosity, heat conduction and species diffusion) were neglected. In Article 2, a method to include the heat conduction terms into the Lagrangian framework is presented. Additionally, the variation of the pressure associated with the fluid particle due to chemical reactions is also neglected. This is a valid assumption, since we are interested only in the evolution of the fluid particle till ignition, during which time the pressure change due to chemical reactions will be small. For the purpose of the present discussion, all diffusive terms in the energy and species mass balance equations are neglected. Most importantly, all terms in the RHS of Equation (2.75) are evaluated at the instantaneous temperature (T) and pressure (p) of the fluid particle at t^*.

To obtain closure for the Lagrangian particle tracking, the particle position and the species production rates need to be obtained. These are governed by the species mass balance and the kinematic equations

$$\frac{DY_i}{Dt^*} = \frac{\mathrm{MW}_i \dot{\omega}_i}{\rho}, \tag{2.76}$$

$$\frac{Dx^*}{Dt^*} = u(t^*). \tag{2.77}$$

The instantaneous pressure and velocity associated with the particle at time t^*, which are required to compute the RHS of Equations (2.75), (2.76) and (2.77), are given by a linear combination of the mean and the fluctuations induced by the disturbances:

$$\begin{aligned} u(t^*) &= u_0(x^*) + \underbrace{\mathrm{e}^{\mathrm{i}\omega(t_i+t^*)}\left(\frac{A}{\rho_0 c_0}\mathrm{e}^{-\mathrm{i}\omega x^*/c_0(1+M_0)} - \frac{B}{\rho_0 c_0}\mathrm{e}^{\mathrm{i}\omega x^*/c_0(1-M_0)}\right)}_{u'(t^*)}, \\ p(t^*) &= p_0(x^*) + \underbrace{\mathrm{e}^{\mathrm{i}\omega(t_i+t^*)}\left(A\mathrm{e}^{-\mathrm{i}\omega x^*/c_0(1+M_0)} + B\mathrm{e}^{\mathrm{i}\omega x^*/c_0(1-M_0)}\right)}_{p'(t^*)}, \end{aligned} \tag{2.78}$$

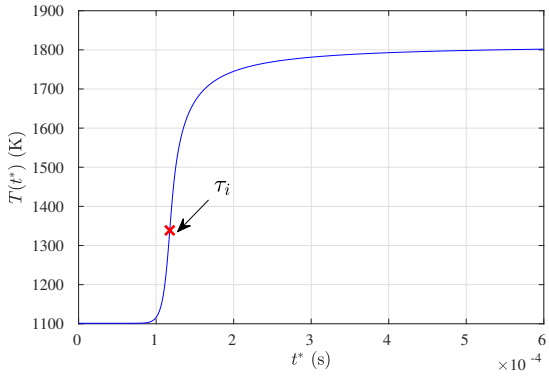

Figure 2.7: Sample graph showing the temperature evolution $T(t^*)$ of a fluid particle.

where A and B are the Fourier transform of the pressure fluctuations associated with the downstream-traveling and upstream-traveling acoustic waves, respectively, at the inlet. These disturbance quantities are assumed to be the inputs to the Lagrangian framework. The angular frequency of the imposed disturbances is given by ω, and M_0 is the mean flow Mach number.

The second term in the RHS of Equation (2.74) is obtained by differentiating the equation governing the temperature fluctuations induced by the acoustic and entropy waves at any time, which is given by

$$T'(t^*) = \frac{\gamma - 1}{\gamma} \frac{T_0}{p_0} p'(t^*) - \frac{T_0}{\rho_0} S_1 e^{i\omega(t_i + t^*)} e^{-i\omega x^*/u_0}, \tag{2.79}$$

where S_1 is the Fourier transform of the density fluctuations induced by the entropy wave at $x = 0$.

Integration of Equations (2.74), (2.76) and (2.77) yields the particle temperature $T(t^*)$. A sample plot of this variation for a particle is given in Figure 2.7. The temperature exhibits a sharp rise at a specific time (τ_i), which signifies the time taken for the particle to ignite from the moment it is injected. The ignition location of this particle is given by $x^*(t^* = \tau_i)$. Therefore, performing the Lagrangian computation for the fluid particle which was injected at time t_i, yields that this particle ignites τ_i seconds after it is injected at a location $x^*(\tau_i)$. Therefore, the location of the autoignition front (X_{ig}) is given by

$$X_{ig}(t_i + \tau_i) = x^*(\tau_i). \tag{2.80}$$

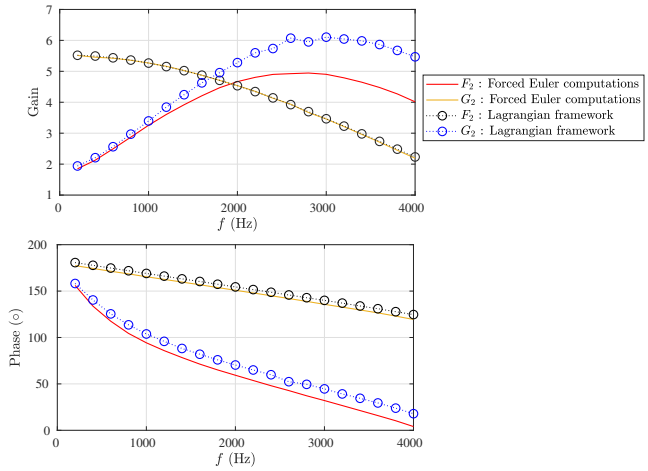

Figure 2.8: Gain and Phase of the flame transfer functions F_2 and G_2 computed from the Lagrangian framework and compared with the forced Euler computations.

Repeating the above process for various particles injected at different time instants t_i, provides the global ignition front response as a function of time. From this data, the instantaneous heat release rate response of the autoignition front can be computed using

$$\dot{Q}(t) = \dot{m}_f \Delta h_c = \rho \Delta h_c (u - u_s)\,, \tag{2.81}$$

where $\dot{m}_f$ is the mass flow rate of the reactants consumed by the autoignition front, u_s is the velocity of the flame front in the laboratory frame of reference, and ρ, u are the instantaneous density and velocity values at the ignition front. The ignition front velocity in the lab frame of reference can be obtained from the ignition front location using

$$u_s = \frac{dX_{\text{ig}}}{dt}. \tag{2.82}$$

The validation of this Lagrangian flame response framework is presented in Article 1, where the flame response predicted by the Lagrangian framework is compared with results from DNS computations. These computations were performed for the one-dimensional configuration in the low-frequency range (100 – 1000 Hz). In Article 2, the Lagrangian framework presented in this section is extended to multi-dimensional configurations,

and the results are validated with forced LES computations of an autoignition front in a backward-facing step geometry. These comparisons revealed that the Lagrangian framework performs very well in predicting the flame dynamics in these configurations. In this section, we present a result which is not included in the articles but is, nevertheless, very relevant for this discussion.

Figure 2.8 plots the gain and phase of the transfer functions F_2 and G_2, which represent the thermal response of the autoignition front, in terms of the integrated heat release rate and ignition front position fluctuations, to a g_1 wave. These are the flame transfer functions which govern the linear dynamics of the intrinsic thermoacoustic feedback (see Figure 2.5). The predictions of the Lagrangian framework are compared with forced Euler computations described in Section 2.1. While the ignition length response is predicted to very good accuracy by the Lagrangian framework, the predictions of the heat release rate response deviate from the forced Euler computations, especially at higher frequencies. While the exact reason for the mismatch cannot be pinpointed by the author at this point, a possible reason could be the inaccuracies in Equation (2.81). In Equation (2.81), the effective mass flow consumed by the flame per unit time is given by $\rho(u - dX_{\mathrm{ig}}/dt)$. At higher frequencies, where the thickness of the flame relative to the wavelength of the acoustic wave is no longer negligible, a modification of this equation might be essential.

2.4 Linearized Euler equation solver

In the previous section, a simplified framework to compute the thermal response of the autoignition front to acoustic and convective perturbations was presented. To be able to predict the intrinsic thermoacoustic oscillations using Equation (2.72), simplified tools which are able to predict the acoustic response of the autoignition front are also essential. These tools should be able to, with good accuracy, compute the g_1 wave generated by an unsteady autoignition front. The simplest and most efficient way to do this analytically is to solve the Rankine–Hugoniot jump conditions (Chu, 1953; Chen et al., 2016). These equations are a set of relations linking the flow perturbations upstream and downstream of the ignition front. They are derived by regarding the ignition front as a jump in the mean flow

variables, and can be written in compact form in the frequency domain as

$$\mathbf{M}\begin{bmatrix} f_2 \\ g_1 \\ h_2 \end{bmatrix} = \mathbf{N}\begin{bmatrix} f_1 \\ g_2 \\ h_1 \end{bmatrix} + \mathbf{K}\,\widetilde{\dot{Q}} + \mathbf{J}\,\widetilde{X}_{\mathrm{ig}}, \tag{2.83}$$

where $\mathbf{M}, \mathbf{N}$ are 3x3 matrices, and $\mathbf{K}, \mathbf{J}$ are 3x1 vectors. The elements of the matrices $\mathbf{M}$, $\mathbf{N}$ and the vectors $\mathbf{K}$, $\mathbf{J}$ are given in the Appendix of Article 3.

While this analytical approach has been used recently in the work of Gant et al. (2020a) to compute the transfer matrix of an autoignition front, a few key aspects are unclear, which are discussed next.

1. **Effect of thin flame approximation**: In the Rankine–Hugoniot approach, the ignition front is regarded as a discontinuous jump in the mean flow variables. This approximation is reasonable for low-frequency acoustic wave propagation, where the wavelength of the acoustic waves are much longer than the ignition front thickness. However, longitudinal ITA modes associated with autoignition fronts need not occur at low frequencies. Euler and DNS computations revealed that at certain conditions, the frequencies of the ITA modes can be as high as 2500 Hz. At these frequencies, the thickness of the ignition front is no longer negligible in comparison to the acoustic wavelength. Furthermore, entropy disturbances are characterized by wavelengths which are smaller than the wavelengths of the acoustic disturbances. Therefore, to capture the correct generation of entropy disturbances from the ignition front, proper resolution of the ignition front might be essential. Indeed, the recent papers of Meindl et al. (2021) and Heilmann et al. (2022) show that inconsistent resolution of the mean flow quantities can result in the spurious generation of entropy perturbations from linearized frameworks.

2. **The presence of gas property fluctuations due to ignition front motion**: Ignition fronts which harmonically oscillate in time, in addition to causing heat release rate perturbations, also cause fluctuations in gas properties. This is illustrated in Figure 2.9, where the back and forth movement of the ignition front results in a back and forth translation of the gas property profiles, which creates gas property fluctuations.

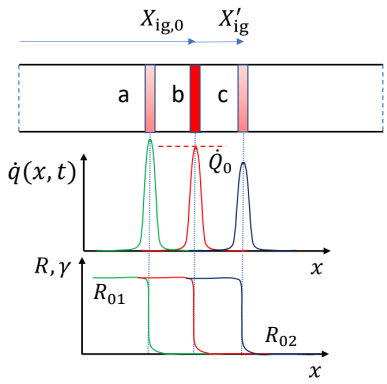

Figure 2.9: Schematic illustrating fluctuations in gas properties and heat release rate due to ignition front motion.

Both propagation and autoignition fronts respond unsteadily to perturbations induced by acoustic disturbances by harmonically changing their position. For flames stabilized by propagation, the fluctuations in the flame position are due to local velocity oscillations kinematically modulating the flame position. In other words, for a freely propagating flame in a 1D duct, the flame will move in accordance with the acoustic forcing:

$$X'_{ig} = \int_0^t u'(X_{ig0}, t)\, dt. \tag{2.84}$$

If the velocity disturbances induced by an acoustic wave are small, the flame position fluctuations will also be small. For autoignition fronts, in addition to the kinematic effect, the flame position fluctuations are created by an additional altogether different mechanism, i.e., modulation of the ignition chemistry by the temperature and pressure perturbations. Even for small values of these perturbations, the ignition length fluctuations need not necessarily be small (see Figure 1.8). This is because of the the modulation of the ignition chemistry by the acoustic temperature fluctuations, resulting in significant fluctuations in the ignition time. Therefore, the effect of gas property fluctuations can be especially relevant for autoignition fronts. The influence of gas property fluctuations cannot be trivially incorporated in the analytical Rankine–Hugoniot framework.

To overcome these drawbacks of the Rankine–Hugoniot approach, in this

work, the acoustic field generated by autoignition fronts is computed using a time-domain linearized Euler equation (LEE) solver. This approach involves in numerically solving the LEE by specifying the boundary conditions and the time-dependent source terms.

The linearized Euler equations can be written by applying the ansatz

$$\Phi(x,t) = \Phi_0(x) + \epsilon\Phi'(x,t) \tag{2.85}$$

to any flow variable or gas property (Φ) into the Euler equations (2.1). Separating out terms which are $O(\epsilon)$ gives the linearized Euler equations which can be written as

$$\begin{aligned}
\frac{\partial \rho'}{\partial t} + \rho_0\frac{\partial u'}{\partial x} + \rho'\frac{\partial u_0}{\partial x} + u_0\frac{\partial \rho'}{\partial x} + u'\frac{\partial \rho_0}{\partial x} &= 0,\\
\frac{\partial u'}{\partial t} + u_0\frac{\partial u'}{\partial x} + u'\frac{\partial u_0}{\partial x} - \frac{\rho'}{\rho_0^2}\frac{\partial p_0}{\partial x} + \frac{1}{\rho_0}\frac{\partial p'}{\partial x} &= 0,\\
\frac{\partial p'}{\partial t} + u_0\frac{\partial p'}{\partial x} + u'\frac{\partial p_0}{\partial x} + \gamma_0 p_0\frac{\partial u'}{\partial x} + \gamma_0 p'\frac{\partial u_0}{\partial x}&\\
-\gamma_0\rho_0 T_0 u'\frac{\partial R_0}{\partial x} - \gamma_0\rho_0 u_0 T'\frac{\partial R_0}{\partial x} - \gamma_0\rho' T_0 u_0\frac{\partial R_0}{\partial x} &= (\gamma_0 - 1)\dot{q}'\\
+\left\{\gamma'\dot{q}_0 - \gamma' p_0\frac{\partial u_0}{\partial x} + \gamma_0\rho_0 T_0\frac{\partial R'}{\partial t} + \gamma_0\rho_0 T_0 u_0\frac{\partial R'}{\partial x} + \gamma'\rho_0 T_0 u_0\frac{\partial R_0}{\partial x}\right\},&
\end{aligned} \tag{2.86}$$

along with the linearized ideal gas equation of state

$$p' = \rho_0 R_0 T' + \rho_0 R' T_0 + \rho' R_0 T_0. \tag{2.87}$$

The boundary conditions for the LEE are imposed in an analogous manner to the procedure employed to impose the boundary conditions for the Euler equations (see Section 2.1). The locally one-dimensional inviscid (LODI) equations (2.9) at the boundary points are first linearized (also see Appendix A) to give

$$\begin{aligned}
\frac{\partial \rho'}{\partial t} + \frac{1}{c_0^2}\left(\mathscr{L}_2' + \frac{1}{2}(\mathscr{L}_1' + \mathscr{L}_5')\right) &= 0,\\
\frac{\partial u'}{\partial t} + \frac{1}{2\rho_0 c_0}(\mathscr{L}_5' - \mathscr{L}_1') &= 0,\\
\frac{\partial p'}{\partial t} + \frac{1}{2}(\mathscr{L}_1' + \mathscr{L}_5') &= (\gamma_0 - 1)\dot{q}',
\end{aligned} \tag{2.88}$$

where the expressions for the linearized versions of the characteristic wave amplitudes ($\mathscr{L}_i'$), which propagate from the interior of the computational domain towards the boundaries, are

$$\begin{aligned}
\mathscr{L}_1' &= (u_0 - c_0)\left(\frac{\partial p'}{\partial x} - \rho_0 c_0 \frac{\partial u'}{\partial x}\right), \\
\mathscr{L}_2' &= u_0\left(c_0^2 \frac{\partial \rho'}{\partial x} - \frac{\partial p'}{\partial x}\right), \\
\mathscr{L}_5' &= (u_0 + c_0)\left(\frac{\partial p'}{\partial x} + \rho_0 c_0 \frac{\partial u'}{\partial x}\right).
\end{aligned} \tag{2.89}$$

Acoustic and entropy forcing at the boundaries are realized by appropriately specifying the amplitudes of the incoming characteristic waves. If we denote the time-varying target values of fluctuations due to the downstream traveling acoustic wave at the inlet, the downstream traveling entropy wave at the inlet and the upstream traveling acoustic wave at the exit as $p'_{\text{in}}(t)$, $\rho'_{\text{in}}(t)$ and $p'_{\text{out}}(t)$, respectively. The wave amplitudes to achieve these target fluctuations are imposed in the form of relaxation terms (Poinsot and Lele, 1992) given by

$$\begin{aligned}
\mathscr{L}_5'(0,t) &= -2\frac{\partial p'_{\text{in}}}{\partial t} + 2K(p' - p'_{\text{in}} - p'_{-}), \\
\mathscr{L}_2'(0,t) &= -c_0^2\frac{\partial \rho'_{\text{in}}}{\partial t} + Kc_0^2(\rho' - \rho'_{\text{in}} - \rho'_{-} - \rho'_{L5}), \\
\mathscr{L}_1'(l,t) &= -2\frac{\partial p'_{\text{out}}}{\partial t} + 2K(p' - p'_{\text{out}} - p'_{+}),
\end{aligned} \tag{2.90}$$

where K is a constant relaxation parameter akin to an inverse time constant with the unit 1/s, p'_{-} and ρ'_{-} are the pressure and density fluctuations induced at the inlet due to the upstream traveling acoustic wave $\mathscr{L}_1$, p'_{+} is the pressure fluctuation induced at the exit by the downstream traveling acoustic wave $\mathscr{L}_5$, ρ'_{L5} is the density fluctuation induced at the inlet by the downstream traveling acoustic wave $\mathscr{L}_5$. These quantities can be

computed by a simple time integration as follows

$$\begin{aligned} p'_- &= -\frac{1}{2}\int_0^t \mathscr{L}'_1(0,t)dt, \\ \rho'_- &= p'_-/c_0^2, \\ p'_+ &= -\frac{1}{2}\int_0^t \mathscr{L}'_5(l,t)dt, \\ \rho'_{L5} &= -\frac{1}{2c_0^2}\int_0^t \mathscr{L}'_5(0,t)dt. \end{aligned} \tag{2.91}$$

Therefore, to impose the boundary conditions, Equation (2.88) is solved at the boundary points in a time-dependent manner. The wave amplitudes approaching the computational domain are specified using Equation (2.90), while the wave amplitudes propagating away from the computational domain are computed using Equation (2.89) and the interior data. These boundary conditions, along with the LEE at the interior points, are then numerically marched in time to get the flow fluctuations. The discretization of the governing equations in space and time are performed using the dispersion relation preserving scheme (Tam et al., 1993), previously discussed in Section 2.1.2.

The final point to discuss is the construction of the source terms in the linearized energy equation and the mean flow profiles. To allow us to time-march the LEE, specification of the mean flow profiles and time-dependent source terms are essential. In the following, we propose a method to construct these quantities using the following inputs: mean values of the primitive variables on either side of the ignition front, the position ($X_{\mathrm{ig}0}$) and the thickness (η) of the ignition front, and the integrated heat release rate and ignition front position fluctuations. The mean quantities can be obtained, for example, from an unforced Euler/DNS computation or a RANS solution. The integrated heat release rate and ignition front position fluctuations are arbitrary inputs, which are specified as inputs in order to compute the frequency response functions S_1 and S_2.

The spatial variation of the mean heat release rate can be constructed by assuming a Gaussian model for the heat release rate distribution (Gant et al., 2020b) as

$$\dot{q}_0(x) = \frac{\dot{Q}_0}{\eta\sqrt{2\pi}} \exp\left(-\frac{(x - X_{\mathrm{ig}0})^2}{2\eta^2}\right), \tag{2.92}$$

where η represents the thickness parameter of the ignition front, and $\dot{Q}_0$ is the mean integrated heat release rate given by

$$\dot{Q}_0 = \frac{\gamma}{\gamma - 1}(u_{02}p_{02} - u_{01}p_{01}) + \frac{1}{2}(\rho_{02}u_{02}^3 - \rho_{01}u_{01}^3), \tag{2.93}$$

where $()_{01}$ and $()_{02}$ denote mean quantities on the unburnt and burnt side, respectively. The instantaneous heat release rate at any time instant t is given by

$$\dot{q}(x,t) = \frac{\dot{Q}_0 + \epsilon\dot{Q}'}{\eta\sqrt{2\pi}} \exp\left(-\frac{(x - X_{ig0} - \epsilon X'_{ig})^2}{2\eta^2}\right), \tag{2.94}$$

where ϵ is a small parameter, and $\dot{Q}', X'_{ig}$ are the integrated heat release rate and ignition length oscillations, which are inputs which need to be specified. Equation (2.94) is written by making use of the fact that the Gaussian profile translates axially due to ignition front fluctuations and changes in area due to integrated heat release rate oscillations. The linearized form of the fluctuating heat release rate can be obtained by subtracting Equation (2.92) from Equation (2.94), expanding the exponential term in a Taylor series, and then simplifying the resulting expression by only retaining terms which are $O(\epsilon)$ and neglecting all terms of higher order. This procedure yields the following expression for the fluctuating heat release rate:

$$\dot{q}'(x,t) = \exp\left(-\frac{(x - X_{ig0})^2}{2\eta^2}\right)\left\{\frac{\dot{Q}'}{\eta\sqrt{2\pi}} + \frac{Q_0}{\eta\sqrt{2\pi}}\frac{X'_{ig}(x - X_{ig0})}{\eta^2}\right\}. \tag{2.95}$$

This can be visualized as two contributors to heat release rate fluctuations at any given point: (i) due to integrated heat release rate fluctuations, and (ii) due to harmonic ignition front motion, which creates heat release rate fluctuations locally even in the absence of global heat release rate oscillations.

The spatial variation of the mean values of any primitive variable or gas property (Φ) can be constructed from the values of the corresponding variables in the unburnt and burnt side and the ignition front thickness by using a smooth transitional model profile as

$$\Phi_0(x) = \Phi_{01} + \frac{1}{2}(\Phi_{02} - \Phi_{01})\left(1 + \mathrm{erf}\,\frac{x - X_{ig0}}{\eta}\right). \tag{2.96}$$

To construct the fluctuating gas properties at any point at a time instant, the instantaneous value of any gas property (for example, the specific heat

ratio γ) is written utilizing the form of Equation (2.96) as

$$\gamma(x,t) = \gamma_{01} + \frac{1}{2}(\gamma_{02} - \gamma_{01})\left(1 + \text{erf}\,\frac{x - X_{\text{ig0}} - \epsilon X'_{\text{ig}}}{\eta}\right). \tag{2.97}$$

In writing Equation (2.97), it is implicitly assumed that the acoustic and entropy disturbances create negligible changes in gas properties and the main contributing factor to gas property fluctuations is the back and forth movement of the ignition front (therefore, gas property fluctuations are zero everywhere in the domain except in the region close to the ignition front). The linearized fluctuations of the gas property γ can be obtained by subtracting Equation (2.96) (for γ_0) from Equation (2.97), writing the terms involving the error function in terms of its series expansions (Abramowitz and Stegun, 1964), and then only retaining the terms which are of order $O(\epsilon)$. The resulting fluctuations in gas property can be written as

$$\gamma'(x,t) = \frac{1}{\sqrt{\pi}}(\gamma_{02} - \gamma_{01})\left(-\frac{X'_{\text{ig}}}{\eta}\right)\exp\left(-\frac{(x - X_{\text{ig0}})^2}{\eta^2}\right). \tag{2.98}$$

Equations (2.92) and (2.96) for the spatial profiles of the mean heat release rate, primitive variable and gas properties, along with Equations (2.95) and (2.98) describing the fluctuations in heat release rate and gas properties, enable us to time march the LEE to determine the primitive variable fluctuations. Now, this procedure of constructing the source terms and mean profiles using model functions is, evidently, not physical because, the Gaussian profile for the mean heat release rate [Equation (2.92)] and the error function profile for the mean primitives/gas properties [Equation (2.96)] are not actual solutions of the time-averaged non-linear Navier–Stokes/ Euler equations. Nevertheless, this approach of using model profiles, constructed using common mathematical functions, to represent mean flows has been used repeatedly in the past in the context of linear flow instability analysis (for example, Schmid and Henningson (2001) for boundary layers and mixing layers, Oberleithner et al. (2011) for swirling jets, and Manoharan and Hemchandra (2015) for a backward-facing step flow).

Chapter 3

Summary of research articles, conclusions and future work

The aim of this thesis is to gain insight into the occurrence of intrinsic thermoacoustic oscillations in reheat combustors with autoignition fronts and to develop predictive modeling tools to allow the efficient prediction of these oscillations in simplified geometries. In order to achieve this overall goal, four objectives were formulated in Section 1.5. These objectives are accomplished in 4 research articles which are summarized in technical detail next.

Article 1

Response of Auto-Ignition-Stabilized Flames to One-Dimensional Disturbances: Intrinsic Response
Harish S. Gopalakrishnan, Andrea Gruber, and Jonas Moeck
Journal of Engineering for Gas Turbines and Power, Volume 143, Issue 12, 2021

Article 1 contributes to Objective 2 by developing a simplified framework to compute the dynamics of one-dimensional autoignition fronts to acoustic and convective perturbations. The simplified framework is based on Lagrangian particle tracking briefly discussed in Section 2.3. The flow is treated as a collection of independently evolving reacting fluid particles. Each of the fluid particles are evolved in time by integrating the Lagrangian form of the energy and species-mass balance equations. The global flame response over one cycle of acoustic oscillation is computed by stitching to-

gether the evolution of all the particles. This framework is compared with forced DNS computations of autoignition fronts, revealing an excellent match in the predicted flame dynamics. Next, the flame response to upstream traveling acoustic perturbations is computed using this framework. The results show that autoignition fronts are highly sensitive to acoustic temperature fluctuations and exhibit a characteristic frequency-dependent response. Acoustic pressure and velocity fluctuations can either constructively or destructively superpose with temperature fluctuations, depending on the mean pressure and relative phase between the fluctuations.

Article 2

Prediction of autoignition-stabilized flame dynamics in a backward-facing step reheat combustor
Harish S. Gopalakrishnan, Tarjei Heggset, Andrea Gruber, and Jonas Moeck
Presented at the Combustion Institute - Canadian Section, Spring Technical Meeting, 2022, Ottawa

Article 2 is a short conference paper which builds upon the work performed in Article 1. The Lagrangian framework proposed in Article 1 for a one-dimensional configuration is extended to multiple dimensions. The results obtained from this framework are compared to forced LES computations of autoignition fronts stabilized in a backwards-facing step combustor configuration. These results show an excellent match both in terms of the flame surface and the integrated heat release rate. This article also contributes to meeting Objective 2 in Section 1.5.

Article 3

Computation of Intrinsic Instability and Sound Generation From Autoignition Fronts
Harish S. Gopalakrishnan, Andrea Gruber, and Jonas Moeck
Journal of Engineering for Gas Turbines and Power, 2022, published online (https://doi.org/10.1115/1.4055421)

Article 3 meets both Objective 1 (in part) and Objective 3 in Section 1.5. A one-dimensional reactive Euler equation framework is formulated and computationally implemented (see also Section 2.1 in this thesis). This framework is used to compute the initial ignition process of autoigniting mixtures in one-dimensional geometries with very low acoustic reflection. These flow computations revealed the occurrence of intrinsic thermoacous-

tic oscillations, which manifest as harmonic oscillations in heat release rate and ignition front position. Comparison of Euler and Navier–Stokes computations revealed that viscous effects have a relatively minor role on the linear behaviour of these intrinsic thermoacoustic oscillations.

In the second part of Article 3, a simplified framework, based on the linearized Euler equations, to compute the acoustic field in reheat combustors is presented (see also Section 2.4 in this thesis). This framework is validated by means of a comparison to forced DNS computations. Additionally, results from Article 3 indicate that autoignition fronts, by virtue of the back and forth motion in response to acoustic perturbations, create fluctuations in gas properties and significant magnitudes of velocity oscillations locally close to the ignition front.

Article 4

Computation and prediction of intrinsic thermoacoustic oscillations associated with autoignition fronts
Harish S. Gopalakrishnan, Andrea Gruber, and Jonas Moeck
Under consideration for publication in Combustion and Flame

Article 4 meets both Objective 1 and Objective 4 in Section 1.5. In the first part of Article 4, forced computations of the autoignition front in the simplified one-dimensional reheat combustor are performed to demonstrate the occurrence of intrinsic thermoacoustic oscillations. The full 3x3 scattering matrix of the autoignition front is derived from these forced flow computations. All elements of the scattering matrix have a common pole corresponding to a frequency of 2500 Hz and a growth rate of $-75\ s^{-1}$, which characterize the linear dynamics of the ITA feedback. Significantly amplified flame responses are observed when the flow is forced close to the frequency of the ITA mode.

In the second part of Article 4, a theoretical framework used to predict the linear stability of the ITA oscillations is developed (also see Section 2.2). This framework is used, along with the linearized Euler equation solver developed in Article 3, to predict the thermoacoustic eigenvalues. The thermoacoustic eigenvalues predicted using this approach showed very good agreement with the detailed flow computations.

3.1 Conclusions

This thesis aims to further our understanding of unsteady combustion phenomena in combustors used for power generation in stationary gas turbines. Such systems use a sequential combustor architecture for efficiently burning fuels with high hydrogen contents. In this thesis, thermoacoustic phenomena in the second-stage of a sequential combustor are studied by means of computation and theory. More specifically, a simplified 'academic' reheat combustor configuration was considered, and the dynamics of the intrinsic thermoacoustic feedback were studied in this configuration.

Intrinsic thermoacoustic feedback is caused, in combustion systems with propagation-stabilized flames, when an upstream-traveling acoustic wave generated by the unsteady flame front introduce flow perturbations, which result in a flame response. The unsteady flame response can be caused either by exciting hydrodynamic oscillations or by creating convected equivalence ratio fluctuations or by modulating the flame front kinematics. This unsteady flame response, in turn, generates upstream-traveling acoustic perturbations which close the feedback loop. In combustors containing autoignition fronts, the ITA feedback is caused by the upstream-traveling acoustic disturbances modulating the ignition chemistry by introducing local temperature and pressure perturbations in the reactant mixture. The modulations in the ignition chemistry result in ignition time oscillations, which result in ignition front position fluctuations causing heat release rate oscillations, which in turn generate acoustic disturbances.

The first significant contribution of this work is the demonstration of the occurrence of ITA oscillations in autoignition fronts. Unforced Euler equation computations of autoignition fronts revealed that the ITA mode manifests as harmonic oscillations prior to the establishment of a stable ignition front. Furthermore, it was also shown that these oscillations tend to be unstable at reactant temperatures where the ignition time is highly sensitive to small temperature changes. Forced computations revealed that the ITA mode shows up as a pronounced peak in the scattering matrix of the autoignition front. The second contribution of this work has been the development of simplified frameworks to enable efficient prediction of the ITA oscillations in a simple reheat combustor configuration.

With regards to the simplified frameworks, first, a Lagrangian particle tracking based methodology was developed to compute the unsteady response of autoignition fronts to acoustic and convective perturbations. This framework treats the flow as a collection of independently evolving re-

acting fluid elements, from which the global flame response is computed. Second, a linearized Euler equation framework was developed to accurately calculate the acoustic field generated by unsteady autoignition fronts. Both these approaches compared very well with corresponding results obtained using more detailed approaches such as forced DNS and Euler computations. Armed with these tools, the prediction of the linear stability of the thermoacoustic oscillations was attempted. Consistent spatial resolution of the mean flow profiles and the fluctuating source terms was found to be most essential for obtaining accurate estimates of the thermoacoustic eigenvalue. Nevertheless, the predictions of the intrinsic thermoacoustic eigenvalues from the simplified approaches showed very good agreement with detailed flow computations. This suggests that the tools developed in this work can form a foundation for more sophisticated thermoacoustic stability analysis frameworks for complex industrial scale combustor geometries.

3.2 Future work

In this thesis, prediction of intrinsic thermoacoustic oscillations were performed in a simplified one-dimensional geometry. A natural extension of this work would be to extend the frameworks developed in this thesis to more complicated (and more realistic) industrial-scale combustor geometries. These geometries would feature a number of additional physical mechanisms which were not considered in this work. To name a few, acceleration of entropy perturbations downstream to generate indirect noise, hydrodynamic instabilities, diffusive effects, turbulence, and so on. To make this work applicable to such realistic geometries, the following directions of future work are envisaged.

- Throughout this work, diffusive effects were neglected in all the flow computations and simplified models. While this is valid for the elementary one-dimensional combustor configuration with an autoignition front, this configuration is far from what is observed in an actual engine. In realistic reheat combustors, the stabilization mechanism of reheat flames would be partly due to propagation and partly due to autoignition. Diffusive effects can play a vital role in such a situation. Furthermore, diffusive effects also play an important role in governing the advective transport of entropy fluctuations from the first stage of the sequential combustor to the second stage. Incorporating diffusive and multi-dimensional effects would be most essential for robust models attempting to study the unsteady response of

reheat flames.

- A key observation from this work is the following. *Fine-grained spatial resolution of the mean flow profiles and the time-dependent source terms is most essential to predict the thermoacoustic eigenvalues accurately.* Indeed, Article 4 has shown that, even in the one-dimensional configuration, approximating the flame and flow by analytically constructed profiles resulted in the generation of spurious entropy waves. When a nozzle is present downstream of the autoignition front, these spurious entropy waves can result in the generation of spurious acoustic perturbations, which can impact the stability predictions. Therefore, future work should focus on developing methods to consistently describe the mean flow and the source terms created due to ignition front motion. A first step towards this objective has already been laid out by the work of Avdonin et al. (2019) and Meindl et al. (2021). In their work, instead of adopting the conventional (divide and conquer) path of supplying a flame transfer function to an acoustic solver to compute the thermoacoustic modes, the full Navier–Stokes equations (including the chemical source terms) were linearized. However, these works used a simple global two-step reaction mechanism. More work is needed to extend this framework to complex reaction mechanisms such as the ones used in this work.

- Throughout this work, vorticity perturbations were neglected. This was done keeping in mind that the main objective of this work was to get insight into the interactions between acoustic waves and the autoignition front. However, realistic reheat combustors have flame-stabilization mechanisms such as bluff-bodies and swirling flows, which are a strong source of hydrodynamic instabilities. Future work should focus on studying the interaction between the autoignition front and vorticity perturbations in a turbulent flow.

- The Lagrangian framework used in this work predicts the ignition front response to acoustic perturbations with excellent accuracy. However, the result of Figure 2.8 shows that at high frequencies, the accuracy of the heat release response prediction decreases. While the precise reasons for this behaviour is unknown at this point, we believe that the finite thickness of the ignition front could become important at higher frequencies, warranting modifications to Equation (2.81). More work is required to improve the predictions at higher frequencies.

Bibliography

Abramowitz, M. and Stegun, I. A. (1964). *Handbook of mathematical functions with formulas, graphs, and mathematical tables*, volume 55. US Government printing office.

Aditya, K., Gruber, A., Xu, C., Lu, T., Krisman, A., Bothien, M. R., and Chen, J. H. (2019). Direct numerical simulation of flame stabilization assisted by autoignition in a reheat gas turbine combustor. *Proceedings of the Combustion Institute*, 37(2):2635–2642.

Æsøy, E. (2022). *The Effect of Hydrogen Enrichment on the Thermoacoustic Behaviour of Lean Premixed Flames*. PhD thesis, NTNU.

Æsøy, E., Aguilar, J. G., Wiseman, S., Bothien, M. R., Worth, N. A., and Dawson, J. R. (2020). Scaling and prediction of transfer functions in lean premixed H2/CH4-flames. *Combustion and Flame*, 215:269–282.

Avdonin, A., Meindl, M., and Polifke, W. (2019). Thermoacoustic analysis of a laminar premixed flame using a linearized reactive flow solver. *Proceedings of the Combustion Institute*, 37(4):5307–5314.

Bauerheim, M., Nicoud, F., and Poinsot, T. (2015). Theoretical analysis of the mass balance equation through a flame at zero and non-zero Mach numbers. *Combustion and Flame*, 162(1):60–67.

Bomberg, S., Emmert, T., and Polifke, W. (2015). Thermal versus acoustic response of velocity sensitive premixed flames. *Proceedings of the Combustion Institute*, 35(3):3185–3192.

Bothien, M., Lauper, D., Yang, Y., and Scarpato, A. (2019a). Reconstruction and analysis of the acoustic transfer matrix of a reheat flame from

large-eddy simulations. *Journal of Engineering for Gas Turbines and Power*, 141(2).

Bothien, M. R., Ciani, A., Wood, J. P., and Fruechtel, G. (2019b). Sequential combustion in gas turbines: the key technology for burning high hydrogen contents with low emissions. In *Turbo Expo: Power for Land, Sea, and Air*, volume 58615, page V04AT04A046. American Society of Mechanical Engineers.

Bothien, M. R., Ciani, A., Wood, J. P., and Fruechtel, G. (2019c). Toward decarbonized power generation with gas turbines by using sequential combustion for burning hydrogen. *Journal of Engineering for Gas Turbines and Power*, 141(12).

Burcat, A. and Ruscic, B. (2005). Third millenium ideal gas and condensed phase thermochemical database for combustion (with update from active thermochemical tables). Technical report, Argonne National Lab.(ANL), Argonne, IL (United States).

Buschmann, P. E., Mensah, G. A., and Moeck, J. P. (2020). Intrinsic thermoacoustic modes in an annular combustion chamber. *Combustion and Flame*, 214:251–262.

Chen, L. S., Bomberg, S., and Polifke, W. (2016). Propagation and generation of acoustic and entropy waves across a moving flame front. *Combustion and Flame*, 166:170–180.

Chu, B.-T. (1953). On the generation of pressure waves at a plane flame front. In *Symposium (International) on Combustion*, volume 4, pages 603–612. Elsevier.

Ciani, A., Bothien, M., Bunkute, B., Wood, J., and Früchtel, G. (2019). Superior fuel and operational flexibility of sequential combustion in Ansaldo Energia gas turbines. *Journal of the Global Power and Propulsion Society*, 3:630–638.

Ciani, A., Wood, J. P., Wickström, A., Rørtveit, G. J., Steeneveldt, R., Pettersen, J., Wortmann, N., and Bothien, M. R. (2020). Sequential combustion in Ansaldo Energia gas turbines: The technology enabler for CO2-free, highly efficient power production based on hydrogen. In *Turbo Expo: Power for Land, Sea, and Air*, volume 84126, page V04AT04A041. American Society of Mechanical Engineers.

Conti, J., Holtberg, P., Diefenderfer, J., LaRose, A., Turnure, J. T., and Westfall, L. (2016). International energy outlook 2016 with projections to 2040. Technical report, USDOE Energy Information Administration (EIA), Washington DC, United States.

Daviller, G., Oztarlik, G., and Poinsot, T. (2019). A generalized non-reflecting inlet boundary condition for steady and forced compressible flows with injection of vortical and acoustic waves. *Computers & Fluids*, 190:503–513.

Dincer, I. and Acar, C. (2015). Review and evaluation of hydrogen production methods for better sustainability. *International Journal of Hydrogen Energy*, 40(34):11094–11111.

Dowling, A. P. (1995). The calculation of thermoacoustic oscillations. *Journal of Sound and Vibration*, 180(4):557–581.

Emmert, T., Bomberg, S., and Polifke, W. (2015). Intrinsic thermoacoustic instability of premixed flames. *Combustion and Flame*, 162(1):75–85.

Gant, F., Bunkute, B., and Bothien, M. R. (2020a). Reheat flames response to entropy waves. *Proceedings of the Combustion Institute*.

Gant, F., Cuquel, A., and Bothien, M. R. (2022). Autoignition flame transfer matrix: analytical model versus large eddy simulations. *International Journal of Spray and Combustion Dynamics*, 14(1-2):72–81.

Gant, F., Gruber, A., and Bothien, M. R. (2020b). Development and validation study of a 1D analytical model for the response of reheat flames to entropy waves. *Combustion and Flame*, 222:305–316.

Goodwin, D. G., Moffat, H. K., Schoegl, I., Speth, R. L., and Weber, B. W. (2022). Cantera: An object-oriented software toolkit for chemical kinetics, thermodynamics, and transport processes. https://www.cantera.org. Version 2.6.0.

Gopalakrishnan, H. S., Gruber, A., and Moeck, J. (2021). Response of auto-ignition-stabilized flames to one-dimensional disturbances: Intrinsic response. *Journal of Engineering for Gas Turbines and Power*, 143(12):121011.

Gruber, A., Bothien, M. R., Ciani, A., Aditya, K., Chen, J. H., and Williams, F. A. (2021). Direct numerical simulation of hydrogen combustion at auto-ignitive conditions: Ignition, stability and turbulent reaction-front velocity. *Combustion and Flame*, 229:111385.

Gustafsson, B. (2007). *High order difference methods for time dependent PDE*, volume 38. Springer Science & Business Media, Berlin, DE.

Hedstrom, G. (1979). Nonreflecting boundary conditions for nonlinear hyperbolic systems. *Journal of Computational Physics*, 30(2):222–237.

Heilmann, G., Liu, T., Romero Vega, P., and Sattelmayer, T. (2022). A novel decomposition approach preventing spurious entropy generation in hybrid thermoacoustic stability computations. *Journal of Engineering for Gas Turbines and Power*, 144(9):091013.

Hemchandra, S., Shanbhogue, S., Hong, S., and Ghoniem, A. F. (2018). Role of hydrodynamic shear layer stability in driving combustion instability in a premixed propane-air backward-facing step combustor. *Physical Review Fluids*, 3(6):063201.

Hoeijmakers, M., Kornilov, V., Arteaga, I. L., de Goey, P., and Nijmeijer, H. (2014). Intrinsic instability of flame–acoustic coupling. *Combustion and Flame*, 161(11):2860–2867.

Kennedy, C. A. and Carpenter, M. H. (1994). Several new numerical methods for compressible shear-layer simulations. *Applied Numerical Mathematics*, 14(4):397–433.

Komarek, T. and Polifke, W. (2010). Impact of swirl fluctuations on the flame response of a perfectly premixed swirl burner. *Journal of Engineering for Gas Turbines and Power*, 132(6).

Kopitz, J. and Polifke, W. (2008). CFD-based application of the Nyquist criterion to thermo-acoustic instabilities. *Journal of Computational Physics*, 227(14):6754–6778.

Lefebvre, A. H. and Ballal, D. R. (2010). *Gas turbine combustion: alternative fuels and emissions*. CRC press, Boca Raton, FL.

LeVeque, R. J. (2002). *Finite volume methods for hyperbolic problems*, volume 31. Cambridge university press, New York, USA.

Li, J., Zhao, Z., Kazakov, A., and Dryer, F. L. (2004). An updated comprehensive kinetic model of hydrogen combustion. *International Journal of Chemical Kinetics*, 36(10):566–575.

Lieuwen, T., McDonell, V., Petersen, E., and Santavicca, D. (2008). Fuel flexibility influences on premixed combustor blowout, flashback, autoignition, and stability. *Journal of Engineering for Gas Turbines and Power*, 130(1).

Lieuwen, T. C. and Yang, V. (2005). *Combustion instabilities in gas turbine engines: operational experience, fundamental mechanisms, and modeling*. Vol 210 of Progress in Astronautics and Aeronautics, American Institute of Aeronautics and Astronautics, Reston, Virginia.

Manoharan, K. and Hemchandra, S. (2015). Absolute/convective instability transition in a backward facing step combustor: Fundamental mechanism and influence of density gradient. *Journal of Engineering for Gas Turbines and Power*, 137(2).

Marble, F. and Candel, S. (1977). Acoustic disturbance from gas nonuniformities convected through a nozzle. *Journal of Sound and Vibration*, 55(2):225–243.

McClure, J., Bothien, M. R., and Sattelmayer, T. (2022). High-frequency mode shape dependent flame-acoustic interactions in reheat flames. *Journal of Engineering for Gas Turbines and Power*.

McManus, K., Poinsot, T., and Candel, S. M. (1993). A review of active control of combustion instabilities. *Progress in Energy and Combustion Science*, 19(1):1–29.

Meindl, M., Silva, C. F., and Polifke, W. (2021). On the spurious entropy generation encountered in hybrid linear thermoacoustic models. *Combustion and Flame*, 223:525–540.

Moeck, J. P., Bourgouin, J.-F., Durox, D., Schuller, T., and Candel, S. (2012). Nonlinear interaction between a precessing vortex core and acoustic oscillations in a turbulent swirling flame. *Combustion and Flame*, 159(8):2650–2668.

Nicoud, F., Benoit, L., Sensiau, C., and Poinsot, T. (2007). Acoustic modes in combustors with complex impedances and multidimensional active flames. *AIAA journal*, 45(2):426–441.

Noiray, N., Durox, D., Schuller, T., and Candel, S. (2008). A unified framework for nonlinear combustion instability analysis based on the flame describing function. *Journal of Fluid Mechanics*, 615(1):139–167.

Oberleithner, K., Schimek, S., and Paschereit, C. O. (2015a). Shear flow instabilities in swirl-stabilized combustors and their impact on the amplitude dependent flame response: A linear stability analysis. *Combustion and Flame*, 162(1):86–99.

Oberleithner, K., Sieber, M., Nayeri, C., Paschereit, C., Petz, C., Hege, H.-C., Noack, B., and Wygnanski, I. (2011). Three-dimensional coherent structures in a swirling jet undergoing vortex breakdown: stability analysis and empirical mode construction. *Journal of Fluid Mechanics*, 679:383–414.

Oberleithner, K., Stöhr, M., Im, S. H., Arndt, C. M., and Steinberg, A. M. (2015b). Formation and flame-induced suppression of the precessing vortex core in a swirl combustor: experiments and linear stability analysis. *Combustion and Flame*, 162(8):3100–3114.

Orchini, A., Silva, C. F., Mensah, G. A., and Moeck, J. P. (2020). Thermoacoustic modes of intrinsic and acoustic origin and their interplay with exceptional points. *Combustion and Flame*, 211:83–95.

Paschereit, C., Schuermans, B., and Campos-Delgado, D. (2001). Active combustion control using an evolution algorithm. In *39th Aerospace Sciences Meeting and Exhibit*, page 783. American Institute of Aeronautics and Astronautics.

Pennell, D. A., Bothien, M. R., Ciani, A., Granet, V., Singla, G., Thorpe, S., Wickstroem, A., Oumejjoud, K., and Yaquinto, M. (2017). An introduction to the Ansaldo GT36 constant pressure sequential combustor. In *Turbo Expo: Power for Land, Sea, and Air*, volume 50855, page V04BT04A043. American Society of Mechanical Engineers.

Poinsot, T. (2017). Prediction and control of combustion instabilities in real engines. *Proceedings of the Combustion Institute*, 36(1):1–28.

Poinsot, T. and Veynante, D. (2005). *Theoretical and numerical combustion*. RT Edwards, Inc., Philadelphia, USA.

Poinsot, T. J. and Lele, S. (1992). Boundary conditions for direct simulations of compressible viscous flows. *Journal of Computational Physics*, 101(1):104–129.

Polifke, W., Wall, C., and Moin, P. (2006). Partially reflecting and non-reflecting boundary conditions for simulation of compressible viscous flow. *Journal of Computational Physics*, 213(1):437–449.

Schmid, P. J. and Henningson, D. S. (2001). *Stability and transition in shear flows*, volume 142. Springer Verlag, New York, USA.

Schuller, T., Durox, D., and Candel, S. (2003). A unified model for the prediction of laminar flame transfer functions: comparisons between conical and V-flame dynamics. *Combustion and flame*, 134(1-2):21–34.

Schulz, O., Doll, U., Ebi, D., Droujko, J., Bourquard, C., and Noiray, N. (2019). Thermoacoustic instability in a sequential combustor: large eddy simulation and experiments. *Proceedings of the Combustion Institute*, 37(4):5325–5332.

Schulz, O. and Noiray, N. (2018). Autoignition flame dynamics in sequential combustors. *Combustion and Flame*, 192:86–100.

Schulz, O. and Noiray, N. (2019). Combustion regimes in sequential combustors: Flame propagation and autoignition at elevated temperature and pressure. *Combustion and Flame*, 205:253–268.

Shreekrishna, Hemchandra, S., and Lieuwen, T. (2010). Premixed flame response to equivalence ratio perturbations. *Combustion Theory and Modelling*, 14(5):681–714.

Silva, C. F., Nicoud, F., Schuller, T., Durox, D., and Candel, S. (2013). Combining a Helmholtz solver with the flame describing function to assess combustion instability in a premixed swirled combustor. *Combustion and Flame*, 160(9):1743–1754.

Staffelbach, G., Gicquel, L., Boudier, G., and Poinsot, T. (2009). Large eddy simulation of self excited azimuthal modes in annular combustors. *Proceedings of the Combustion Institute*, 32(2):2909–2916.

Strahle, W. C. (1971). On combustion generated noise. *Journal of Fluid Mechanics*, 49(2):399–414.

Sutherland, J. C. and Kennedy, C. A. (2003). Improved boundary conditions for viscous, reacting, compressible flows. *Journal of Computational Physics*, 191(2):502–524.

Tam, C. K. (2012). *Computational aeroacoustics: A wave number approach*, volume 33. Cambridge University Press, New York, USA.

Tam, C. K., Webb, J. C., et al. (1993). Dispersion-relation-preserving finite difference schemes for computational acoustics. *Journal of Computational Physics*, 107(2):262–281.

Tay Wo Chong, L., Komarek, T., Kaess, R., Föller, S., and Polifke, W. (2010). Identification of flame transfer functions from LES of a premixed swirl burner. In *Turbo Expo: Power for Land, Sea, and Air*, volume 43970, pages 623–635.

Thompson, K. W. (1987). Time dependent boundary conditions for hyperbolic systems. *Journal of Computational Physics*, 68(1):1–24.

Thompson, K. W. (1990). Time-dependent boundary conditions for hyperbolic systems, ii. *Journal of Computational Physics*, 89(2):439–461.

Turns, S. R. et al. (1996). *Introduction to combustion*, volume 287. McGraw-Hill Companies New York, NY, USA.

Yahou, T., Dawson, J. R., and Schuller, T. (2022). Impact of chamber back pressure on the ignition dynamics of hydrogen enriched premixed flames. *Proceedings of the Combustion Institute*.

Zellhuber, M., Schuermans, B., and Polifke, W. (2014). Impact of acoustic pressure on autoignition and heat release. *Combustion Theory and Modelling*, 18(1):1–31.

Publications in full text

Response of Auto-Ignition-Stabilized Flames to One-Dimensional Disturbances: Intrinsic Response

available in Journal of Engineering For Gas Turbines and Power 2021 ;Volum 143.(12)
https://doi.org/10.1115/1.4052058

Prediction of autoignition-stabilized flame dynamics in a backward-facing step reheat combustor

This paper is awaiting pubicaton and is not included

Computation of Intrinsic Instability and Sound Generation From Autoignition Fronts

Computation and prediction of intrinsic thermoacoustic oscillations associated with autoignition fronts

This paper is awaiting publication and is not included in NTNU Open

Appendix A

Characteristic waves from linearized Euler equations

The Riemann invariants for the flow depicted in Figure 1.7 is derived in this section. We start with the linearized Euler equations at the boundary point which can be written as

$$\frac{\partial}{\partial t}\begin{bmatrix}\rho' \\ u' \\ p'\end{bmatrix} + \begin{bmatrix}u_0 & \rho_0 & 0 \\ 0 & u_0 & 1/\rho_0 \\ 0 & \gamma p_0 & u_0\end{bmatrix}\frac{\partial}{\partial x}\begin{bmatrix}\rho' \\ u' \\ p'\end{bmatrix} = 0 \tag{A.1}$$

In writing the above equation, the fluctuations in the source terms and gas properties are assumed to be zero at the boundary points. This is a valid assumption as these quantities are non-zero only in the region close to the flame front, and the magnitudes of these fluctuations are very small at the boundary points. The above equation can be written in compact form as

$$q_t + \mathbf{A}q_x = 0 \tag{A.2}$$

Applying a similarity transformation to the matrix A results in

$$q_t + \mathbf{R}\Lambda\mathbf{R}^{-1}q_x = 0 \implies \mathbf{R}^{-1}q_t + \Lambda\mathbf{R}^{-1}q_x = 0 \tag{A.3}$$

The eigenvalues and eigenvectors of the matrix $\mathbf{A}$ can be written as

$$\Lambda = \begin{bmatrix} u_0 - c_0 & 0 & 0 \\ 0 & u_0 & 0 \\ 0 & 0 & u_0 + c_0 \end{bmatrix}, \mathbf{R} = \begin{bmatrix} 1 & 1 & 1 \\ -c_0/\rho_0 & 0 & c_0/\rho_0 \\ c_0^2 & 0 & c_0^2 \end{bmatrix}. \tag{A.4}$$

The inverse of the matrix $\mathbf{R}$ is

$$\mathbf{R}^{-1} = \begin{bmatrix} 0 & -\frac{\rho_0}{2c_0} & \frac{1}{2c_0^2} \\ 1 & 0 & -\frac{1}{c_0^2} \\ 0 & \frac{\rho_0}{2c_0} & \frac{1}{2c_0^2} \end{bmatrix}. \tag{A.5}$$

Applying the inverse of the matrix into Equation (A.3) gives the set of three equations, which are

$$\frac{1}{2}\frac{\partial}{\partial t}\left(p' - \rho_0 c_0 u'\right) + \frac{1}{2}(u_0 - c_0)\frac{\partial}{\partial x}\left(p' - \rho_0 c_0 u'\right) = 0$$

$$\frac{\partial}{\partial t}\left(p' - c_0^2 \rho'\right) + u_0 \frac{\partial}{\partial x}\left(p' - c_0^2 \rho'\right) = 0 \tag{A.6}$$

$$\frac{1}{2}\frac{\partial}{\partial t}\left(p' + \rho_0 c_0 u'\right) + \frac{1}{2}(u_0 + c_0)\frac{\partial}{\partial x}\left(p' + \rho_0 c_0 u'\right) = 0.$$

The above equation shows that the characteristic variables W: $p' - \rho_0 c_0 u'$, $p' - c_0^2 \rho'$ and $p' + \rho_0 c_0 u'$ are governed by the equations

$$\frac{DW}{Dt} = 0 \tag{A.7}$$

along the curves given by $dx/dt = u_0 - c_0, u_0, u_0 + c_0$. Therefore, the Riemann invariants are given by

$$\begin{bmatrix} g \\ h \\ f \end{bmatrix} = \begin{bmatrix} \frac{1}{2}(\widetilde{p} - \rho_0 c_0 \widetilde{u}) \\ c_0^2 \widetilde{\rho} - \widetilde{p} \\ \frac{1}{2}(\widetilde{p} + \rho_0 c_0 \widetilde{u}) \end{bmatrix}. \tag{A.8}$$